Novel approaches to improve estimates of short-lived halocarbon emissions during summer from the Southern Ocean using airborne observations

Elizabeth Asher[1], Rebecca S. Hornbrook[1], Britton B. Stephens[1], Doug Kinnison[1], Eric J. Morgan[5], Ralph F. Keeling[5], Elliot L. Atlas[6], Sue M. Schauffler[1], Simone Tilmes[1], Eric A. Kort[2], Martin S. Hoecker-Martínez[3], Matt C. Long[1], Jean-François Lamarque[1], Alfonso Saiz-Lopez[4,1], Kathryn McKain[7,8], Colm Sweeney[8], Alan J. Hills[1], and Eric C. Apel[1]

[1] National Center for Atmospheric Research, Boulder, Colorado, USA

[2] University of Michigan, Climate and Space Sciences and Engineering, Ann Arbor, Michigan, USA

[3] University of Redlands, Physics Department, Redlands, California, USA

[4] Department of Atmospheric Chemistry and Climate, Institute of Physical Chemistry Rocasolano, CSIC, Madrid, Spain

[5] Scripps Institution of Oceanography, University of California, San Diego, California, USA

[6] University of Miami, Department of Atmospheric Sciences, Miami, Florida, USA

[7] Cooperative Institute for Research in Environmental Sciences, University of Colorado, Boulder, Colorado, USA

[8] National Oceanic and Atmospheric Administration, Boulder, Colorado, USA

Abstract.

Fluxes of halogenated volatile organic compounds (HVOCs) over the Southern Ocean remain poorly understood, and few atmospheric measurements exist to constrain modeled emissions of these compounds. We present observations of $CHBr_3$, CH_2Br_2, CH_3I, $CHClBr_2$, $CHBrCl_2$, and CH_3Br during the O_2/N_2 Ratio and CO_2 Airborne Southern Ocean (ORCAS) study and the 2nd Atmospheric Tomography mission (ATom-2), in January and February of 2016 and 2017. Good model-measurement correlations were obtained between these observations and simulations from the Community Earth System Model (CESM) atmospheric component with chemistry (CAM-Chem) for $CHBr_3$, CH_2Br_2, CH_3I, and $CHClBr_2$ but all showed significant differences in model: measurement ratios. The model: measurement comparison for CH_3Br was satisfactory and for $CHBrCl_2$ the low levels present precluded us from making a complete assessment. Thereafter, we demonstrate two novel approaches to estimate HVOC fluxes; the first approach takes advantage of the robust relationships that were found between airborne observations of O_2 and $CHBr_3$, CH_2Br_2, and $CHClBr_2$; we use these linear regressions with observed O_2 and modeled O_2 distributions to infer a biological flux of HVOCs. The second approach uses the Stochastic Time-Inverted Lagrangian Transport (STILT) particle dispersion model to explore the relationships between observed mixing ratios and the product of the upstream surface influence and sea ice, chl a, absorption due to detritus, and downward shortwave radiation at the surface, which in turn relate to various regional hypothesized sources of HVOCs such as marine phytoplankton, phytoplankton in sea ice brines, and decomposing organic matter in surface seawater. These relationships can help evaluate the likelihood of particular HVOC sources, and in the case of statistically significant correlations, such as was found for CH_3I, may be used to derive an estimated flux field. Our results are consistent with a biogenic regional source of $CHBr_3$, and both non-biological and biological sources of CH_3I over these regions.

1 Introduction

Emissions of halogenated volatile organic compounds (HVOCs) influence regional atmospheric chemistry and global climate. Through the production of reactive halogen radicals at high latitudes, HVOCs contribute to tropospheric and stratospheric ozone destruction, and alter the sulfur, mercury, nitrogen oxide and hydrogen oxide cycles (e.g. Schroeder et al., 1998; Boucher et al., 2003; Bloss et al., 2005; von Glasow and Crutzen, 2007; Saiz-Lopez et al., 2007; Obrist et al., 2011; WMO, 2018). In the marine boundary layer and lower troposphere, sea salt is the main source of reactive bromine (Finlayson-Pitts 1982; Simpson et al., 2015). Yet HVOCs may also be a more important source of inorganic bromine to the whole atmosphere than previously thought, according to a recent study, which indicates that sea salt is scarce and insufficient to control the bromine budget in the middle and upper troposphere (Murphy et al., 2019).

Phytoplankton and macroalgae in the ocean are the main sources to the atmosphere of several very short-lived bromocarbons, including bromoform ($CHBr_3$), dibromomethane (CH_2Br_2), dibromochloromethane ($CHClBr_2$), and bromodichloromethane ($CHBrCl_2$) (Moore et al., 1996; Carpenter et al. 2003; Butler et al., 2007; Raimund et al., 2011). Other HVOCs, such as methyl

59 iodide (CH_3I), and methyl bromide (CH_3Br) have many natural sources, such as coastal
60 macroalgae, phytoplankton, temperate forest soil and litter, and biomass burning (e.g., Bell et al.,
61 2002; Sive et al., 2007; Colomb et al. 2008; Drewer et al., 2008). CH_3I is also formed through
62 non-biological reactions in surface seawater, and CH_3Br is emitted as a result of quarantine and
63 pre-shipment activities, which are not regulated by the Montreal Protocol (e.g., Moore and
64 Zafiriou; 1994, WMO 2018). Over the Southern Ocean specifically, hypothesized sources of
65 HVOCs include: coastal macroalgae, phytoplankton, sea ice algae, and photochemical or dust
66 stimulated non-biological production at the sea surface (e.g., Abrahamsson et al. 2018; Manley
67 and Dastoor 1998; Moore and Zafiriou 1994; Moore et al., 1996; Richter and Wallace 2004;
68 Williams et al., 2007; Tokarczyk and Moore 1994; Sturges et al., 1992).

69 We largely owe our current understanding of marine HVOC emissions over the Southern Ocean
70 to ship-based field campaigns and laboratory process studies (e.g., Abrahamsson et al. 2004a,b;
71 Atkinson et al., 2012; Carpenter et al., 2007; Moore et al., 1996; Chuck et al., 2005; Butler et al.,
72 2007; Raimund et al., 2011; Hughes et al., 2009; Mattsson et al. 2013; Hughes et al., 2013).
73 These studies have reported surface water and sea-ice HVOC supersaturation and corresponding
74 elevated levels of HVOCs in the marine boundary layer (MBL) in summer, and have identified
75 numerous biological and non-biological ocean sources for these compounds. Mattsson et al.
76 (2013) noted that the ocean also acts as a sink for HVOCs, when HVOC undersaturated surface
77 waters equilibrate with air masses transported from source regions. The spatially heterogeneous
78 ocean sources of $CHBr_3$ and CH_2Br_2 at high latitudes in the Southern Hemisphere are often
79 underestimated in global atmospheric models (Hossaini et al., 2013; Ordoñez et al., 2012; Ziska
80 et al., 2013). Ship-based and Lagrangian float observations provide invaluable information on
81 the sources and temporal variability of compounds in the surface ocean. These methods offer the
82 advantage of simultaneous measurements of both air and seawater to evaluate the gases'
83 saturation state in the surface ocean and calculate fluxes. Yet ship-based measurements onboard
84 these slow moving platforms also have drawbacks: they under sample the spatial variability of
85 HVOCs (e.g., Butler et al., 2007) and require assumptions about gas-exchange rates to estimate
86 fluxes.

87 To disentangle the roles of atmospheric transport and spatial variability of emissions on HVOC
88 distributions requires large-scale atmospheric observations. At low latitudes, large-scale
89 convection at the intertropical convergence zone carries bromocarbons and other HVOCs into
90 the free troposphere and lower stratosphere (e.g., Liang et al., 2014; Navarro et al., 2015). Polar
91 regions are characterized by stable boundary layers in summer. Wind shear, frontal systems, and
92 internal gravity waves create turbulence and control vertical mixing within and across a stable
93 polar boundary layer (e.g. Anderson et al., 2008), and small, convective plumes may form over
94 the marginal sea ice zone, related to sea ice leads as well as winds from ice-covered to open-
95 ocean waters (e.g. Schnell et al., 1989). As a result of limited vertical transport in these regions,
96 however, air-sea fluxes lead to strong vertical gradients. Zonal transport from lower latitudes has
97 a large impact on the vertical gradients of trace gas mixing ratios over polar regions (Salawitch
98 2010). Given their extended photochemical lifetimes at high latitudes (see Sect. 2.3 for a brief
99 discussion), many HVOC distributions are particularly sensitive to zonal transport at altitude.

100 Aircraft observations can rapidly map basin-wide vertical distributions, support quantitative flux
101 estimates, and provide spatial constraints to atmospheric models (e.g. Xiang et al., 2010;
102 Stephens et al., 2018; Wofsy et al., 2011). Few airborne observations of HVOCs exist at high
103 latitudes in the Southern Hemisphere. Two earlier aircraft campaigns that have measured
104 summertime HVOCs in this region are the first Aerosol Characterization Experiment (ACE-1;
105 Bates et al., 1999) and the first High-performance Instrumented Airborne Platform for
106 Environmental Research (HIAPER) Pole-to-Pole Observations (HIPPO; Wofsy, 2011)
107 campaign. For these two aircraft campaigns, whole air samples were collected onboard the
108 NSF/NCAR C-130 and the NSF/NCAR Gulfstream V (GV) during latitudinal transects over the
109 Pacific Ocean as far south as 60° S and 67° S, respectively. However, the ACE-1 and HIPPO
110 campaigns obtained relatively few whole air samples in this region, with ≤100 samples poleward
111 of 60° S combined (e.g., Blake et al., 1999; Hossaini et al., 2013). ACE-1 measurements of CH_3I
112 in the MBL indicate a strong ocean source between 40° S and 50° S in austral summer, with
113 mixing ratios above 1.2 pmol below ~1 km (Blake et al., 1999).

114 HVOC emissions are frequently incorporated into earth system models, using either
115 climatologies or parameterizations based on satellite observations of chlorophyll and
116 geographical region and evaluated using mixing ratio comparisons with airborne observations. In
117 Section 3.1 and 3.2, we report new airborne observations of $CHBr_3$, CH_2Br_2, CH_3I, $CHClBr_2$,
118 $CHBrCl_2$, and CH_3Br from high latitudes in the Southern Hemisphere, where data are scarce, as
119 well as large-scale regional mixing ratio comparisons for HVOCs with the community earth
120 system model (CESM) atmospheric component with chemistry (CAM-Chem). In section 3.4, we
121 present two novel approaches to estimate regional fluxes of HVOCs for comparison with global
122 climate models' parameterizations or climatologies. One approach uses correlations of HVOCs
123 of marine origin to marine oxygen (O_2), as measured by deviations in the ratio of O_2 to nitrogen
124 (N_2) ($\delta(O_2/N_2)$ see Sect. 2.1.2 and 3.1.2). We exploit robust ratios of HVOCs to oxygen (O_2)
125 determined from linear regressions (i.e. the enrichment ratio), and the ocean flux of O_2 from
126 CESM's ocean component, to estimate the marine biogenic flux of several HVOCs. The second
127 approach relies on observed HVOC mixing ratios, the Stochastic Time-Inverted Lagrangian
128 Transport (STILT) particle dispersion model and geophysical datasets (see Sect. 2.3 and 3.3).
129 We assess contributions from previously hypothesized regional sources for the Southern Ocean,
130 and estimate HVOC fluxes based on regressions between upstream influences and observed
131 mixing ratios and distributions of remotely sensed data.

132

2 Methods

2.1 Measurements

135 Atmospheric measurements for this study were collected at high latitudes in the Southern
136 Hemisphere as part of the O_2/N_2 Ratio and CO_2 Airborne Southern Ocean (ORCAS) study
137 (Stephens et al., 2018), and the second NASA Atmospheric Tomography Mission (ATom-2),
138 near Punta Arenas, Chile (Fig. 1). The ORCAS field campaign took place from Jan. 15 – Feb.
139 29, 2016 onboard the NSF/NCAR GV. On Feb. 10 and 13, 2017 the sixth and seventh ATom-2
140 research flights passed over the eastern Pacific sector poleward of 60° S (defined here as Region

141 1) and over the Patagonian Shelf between 40° S and 55° S and between 70° W and 50° W
142 (defined here as Region 2), respectively. The two regions for this study are defined based
143 loosely on dynamic biogeochemical provinces identified using bathymetry, algal biomass, sea
144 surface temperature and salinity (Reygondeau et al., 2013).

145 Both projects featured en route vertical profiling from near the ocean surface (~ 150 m) to the
146 upper-troposphere, with 74 ORCAS and seven ATom-2 (during the sixth and seventh flights)
147 low-altitude level legs in the MBL. These campaigns shared a number of instruments, including
148 the NCAR Trace Gas Organic Analyzer (TOGA), the NCAR Atmospheric Oxygen (AO2)
149 instrument, a Picarro cavity ringdown spectrometer operated by NOAA, discussed below. More
150 information about individual instruments may be found in Stephens et al., 2018 and at
151 https://www.eol.ucar.edu/field_projects/orcas and https://espo.nasa.gov/atom/content/ATom.

152

2.1.1 Halogenated VOCs

154 During ORCAS and ATom-2 TOGA provided mixing ratios of over 60 organic compounds,
155 including HVOCs. The instrument, described in Apel et al. (2015), continuously collects and
156 analyzes samples for $CHBr_3$, CH_2Br_2, $CHClBr_2$, $CHBrCl_2$, and CH_3I among other compounds,
157 with a 35-second sampling period and repeats the cycle every two-minutes using online fast gas
158 chromatography and mass spectrometry. This study also leverages measurements of CH_3Br from
159 whole air samples from the U. Miami / NCAR Advanced Whole Air Sampler (AWAS;
160 Schauffler et al., 1999) onboard the GV during the ORCAS campaign and the UC Irvine Whole
161 Air Sampler (WAS; Blake et al., 2001) onboard the DC-8 during the ATom-2 campaign.
162 HVOCs reported here have an overall ±15% accuracy and ±3% relative precision, and detection
163 limits of 0.03 ppt for CH_3I, 0.2 ppt for $CHBr_3$, 0.03 ppt for CH_2Br_2, 0.03 ppt for $CHClBr_2$, 0.05
164 ppt for $CHBrCl_2$, and 0.2 ppt for CH_3Br. In addition, comparisons between onboard collected
165 whole air samples and in-flight TOGA measurements, when sharing over half of their sampling
166 period, showed good correlations for $CHBr_3$, CH_2Br_2, CH_3I, and $CHClBr_2$, although there were
167 some calibration differences (Fig. S1 and Fig. S2). In addition to the comparison between co-
168 located atmospheric measurements, we also conducted a lab inter-comparison following the
169 campaign between NOAA's programmable flask package (PFP) and TOGA (Table S1; see
170 supplement for details).

171

2.1.2 $\delta(O_2/N_2)$ and CO_2

173 The AO2 instrument measures variations in atmospheric O_2, which are reported as relative
174 deviations in the oxygen to nitrogen ratio ($\delta(O_2/N_2)$), following a dilution correction for CO_2
175 (Keeling et al., 1998; Stephens et al., 2018). The instrument's precision is ±2 per meg units (one
176 in one million relative) for a 5 second measurement (Stephens et al., 2003; Stephens et al.,
177 manuscript in preparation, 2019). Anthropogenic, biogenic, and oceanic processes introduce O_2
178 perturbations that are superimposed on the background concentrations of O_2 in air (XO_2, in dry
179 air = 0.2095). Air-sea O_2 fluxes are driven by both biological production and consumption of O_2

and by heating and cooling of surface waters. O_2 is consumed when fossil fuels are burned and produced and consumed during terrestrial photosynthesis and respiration. Seasonal changes in the ocean heat content lead to small changes in atmospheric N_2. As others have done, we isolated the air-sea O_2 signal by subtracting model estimates of the terrestrial O_2, fossil-fuel O_2, and air-sea N_2 flux influences from the $\delta(O_2/N_2)$ measurements (Equation 1; Keeling et al., 1998; Garcia and Keeling, 2001; Stephens et al., 2018). The difference of the $\delta(O_2/N_2)$ measurement and these modeled components is multiplied by XO_2 to convert to ppm equivalents as needed (ppm eq; Keeling et al., 1998; Equation 1).

$$O_{2\text{-ppm-equiv}} = [\delta(O_2/N_2) - \delta(O_2/N_2)_{\text{Land}} - \delta(O_2/N_2)_{\text{Fossil Fuel}} - \delta(O_2/N_2)_{N2}] \times XO_2 \qquad (1)$$

We obtained the modeled $\delta(O_2/N_2)$ signal terrestrial influences from the land model component of the CESM, the fossil fuel combustion influences from the Carbon Dioxide Information Analysis Center (CDIAC; Boden et al. 2017), and the air-sea N_2 influences from the oceanic component of CESM. These fluxes were all advected through the specified dynamics version of CESM's atmosphere component, as described below in Sect. 2.2 and in Stephens et al. (2018).

CO_2 measurements were provided by NOAA's Picarro G2401-m cavity ring down spectrometer modified to have a ~1.2 sec measurement interval and a lower cell pressure of 80 Torr, which enabled the instrument to function at the full range of GV altitudes (McKain et al. manuscript in preparation, 2019). Dry-air mole fractions were calculated using empirical corrections to account for dilution and pressure broadening effects as determined in the laboratory before and after the campaign deployments, and in-flight calibrations were used to determine an offset correction for each flight. Corrected CO_2 data have a total average uncertainty of 0.07 ppm (McKain et al. manuscript in preparation, 2019). To merge them with the TOGA data, these faster O_2 and CO_2 measurements were arithmetically averaged over TOGA's 35-s sampling periods (Stephens et al., 2017 and https://espo.nasa.gov/atom/content/ATom).

2.2 CAM-Chem model configuration

The CESM version 1, atmospheric component with chemistry (CAM-Chem) is a global three-dimensional chemistry climate model that extends from the Earth's surface to the stratopause. CAM-Chem version 1.2 includes all the physical parameterizations of Neale et al. (2013) and a finite volume dynamical core (Lin, 2004) for tracer advection. The model has a horizontal resolution of 0.9° latitude × 1.25° longitude, with 56 vertical hybrid levels and a time-step of 30 minutes. Meteorology is specified using the NASA Global Modeling and Assimilation Office (GMAO) Goddard Earth Observing System Model, version 5 (GEOS-5; Rienecker et al., 2008) (GEOS-5), following the specified dynamic procedure described by Lamarque et al. (2012). Winds, temperatures, surface pressure, surface stress, and latent and sensible heat fluxes are nudged using a 5-hour relaxation timescale to GEOS-5 1° × 1° meteorology. The sea surface temperature boundary condition is derived from the Merged Hadley-NOAA Optimal Interpolation Sea Surface Temperature and Sea-Ice Concentration product (Hurrell et al., 2008). The model uses chemistry described by Tilmes et al. (2016), biomass burning and biogenic

220   emissions from the Fire INventory of NCAR (FINN; Wiedinmyer et al., 2011) and MEGAN
221   (Model of Emissions of Gasses and Aerosols from Nature) 2.1 products (Guenther et al., 2012)
222   and additional tropospheric halogen chemistry described in Fernandez et al. (2014) and Saiz-
223   Lopez et al. (2014). These include ocean emissions of $CHBr_3$, CH_2Br_2, $CHBr_2Cl$, and $CHBrCl_2$,
224   with parameterized emissions based on chlorophyll *a* (chl *a*) concentrations and scaled by a
225   factor of 2.5 over coastal regions, as opposed to open ocean regions (Ordoñez et al., 2012). The
226   model used an existing CH_3I flux climatology (Bell et al., 2002), and CH_3Br was constrained to a
227   surface lower boundary condition, also described by Ordoñez et al. (2012). This version of the
228   model was run for the period of the ORCAS field campaign (January and February 2016),
229   following a 24-month spin-up. To facilitate comparisons to ORCAS observations, output
230   included vertical profiles of modeled constituents from the two nearest latitude and two nearest
231   longitude model grid-points (four profiles in total) to the airborne observations at every 30-min
232   model time-step. Following the run, simulated constituent distributions were linearly interpolated
233   to the altitude, latitude and longitude along the flight track, yielding co-located modeled
234   constituents and airborne observations. This version of the model has not yet been run for the
235   ATom-2 period.

236

2.3 STILT model configuration

238   The Stochastic Time-Inverted Lagrangian Transport (STILT; Lin et al., 2003) particle dispersion
239   model uses a receptor oriented framework to infer surface sources or sinks of trace gases from
240   atmospheric observations collected downstream, thus simulating the upstream influences that are
241   ultimately measured at the receptor site. The model tracks ensembles of particle trajectories
242   backward in time and the resulting distributions of these particles can be used to define surface
243   influence maps for each observation. STILT was run using 0.5° Global Data Assimilation System
244   (GDAS) reanalysis winds to investigate the transport history of air sampled along the flight track
245   (Stephens et al., 2018). For each TOGA observation, an ensemble of 4,096 particles was
246   released from the sampling location and followed over a backwards simulation period of seven
247   days. Particles in the lower half of the simulated MBL are assigned a surface influence value,
248   which quantitatively links observed mixing ratios to surface sources (Lin et al., 2003). The
249   average surface influence of all 4,096 particles per sampling location yields an hourly and
250   spatially gridded surface influence value (ppt m^2 s $pmol^{-1}$) at a spatial resolution of 0.25° x 0.25°
251   for each sample point.

252   Uncertainty in the surface influence value is strongly influenced by the accuracy of the
253   underlying meteorological transport, as discussed in Xiang et al. (2010). We evaluated the
254   GDAS reanalysis winds by comparing model winds interpolated in space and averaged between
255   corresponding time points and pressure levels to match aircraft observations. By evaluating
256   differences between observed winds and modeled winds along the flight tracks we can estimate
257   uncertainty in the surface influence values. We consider the observation-model differences in
258   both wind speed and direction to approximate errors in surface influence strength and location.
259   For wind speed, a small bias may be present, where we find a median difference between
260   observations and reanalysis of 0.68 m s^{-1}, a 5% relative bias. The 1-sigma of the wind speed

261   difference is 2.3 m s^{-1}, corresponding to a 19% 1-sigma uncertainty in wind speed. In its
262   simplest approximation, the surface influence strength error is perfectly correlated with the wind
263   speed error, and thus we take 19% as an approximation of the surface influence strength
264   uncertainty. The uncertainty in surface influence location depends on the error in the wind
265   direction. We find a 1-sigma error of 14 degrees in wind speed, which corresponds to a possible
266   error of 260 km day^{-1}.

267   Finally, we note that photochemical loss during transport is not accounted for in this analysis.
268   Low OH mixing ratios, cold temperatures, and lower photolysis rates due to angled sunlight at
269   high latitudes lead to longer than average HVOC lifetimes. For instance, assuming an average
270   diurnal OH concentration of 0.03 ppt, and average photochemical loss according to the
271   Tropospheric Ultraviolet and Visible (TUV) radiation model and the Mainz Spectral data site
272   (http://satellite.mpic.de/spectral_atlas) for Jan. 29 under clear sky conditions at 60° S, $CHBr_3$ has
273   a lifetime of 30 days, CH_2Br_2 has a lifetime of 270 days, CH_3I has a lifetime of 7 days, and
274   $CHClBr_2$ has a lifetime of 63 days. As such, the photochemical lifetimes of these gases are
275   greater than or equal to the time of our back-trajectory analysis. Moreover, OH concentrations in
276   this region have large uncertainties, the inclusion of which would lead to more, not less,
277   uncertainty in surface influence based regression coefficients and estimated fluxes (see Sect. 2.3
278   and 3.3 for details).

279

280   **2.3.1 STILT surface influence functions**

281   For this study, we used STILT surface influence distributions with remotely sensed ocean
282   surface and reanalysis data (i.e. surface source fields) in linear and multi-linear regressions to
283   generate empirical STILT influence functions.   Surface influence functions can help explain
284   observed mixing ratios of $CHBr_3$, CH_2Br_2, CH_3Br and CH_3I, evaluate the likelihood of particular
285   HVOC sources, and in the case of statistically significant correlations, may be used to derive an
286   estimated flux field (See Sect. 3.3 and 3.4.2 for details).

287

288   We tested whether observed mixing ratios (Z) could be explained by a linear relationship in
289   which the predictor variable is a surface influence function, equal to the product of the surface
290   influence (H) and a potential geophysical surface source field(s), such as chl a, as well as an
291   intercept (b), a slope (a), and error term ξ (Equation 2; Fig. S5). This relationship can be
292   generalized as a multiple linear regression with multiple surface influence functions (Hs_1, Hs_2…)
293   and slope coefficients (a_1, a_2; Equation 3), when multiple sources contribute to observed HVOC
294   mixing ratios. The multiple linear regression may also include an interaction term (Hs_1Hs_2)
295   between predictor variables (e.g. Hs_1 and Hs_2) with a slope coefficient (a_3) to improve the fit.
296   Statistical correlations between mixing ratios and surface influence functions may be used to
297   support or reject hypothesized sources. A flux (μmol m^{-2} s^{-1}) may then be estimated for each grid
298   cell based on the product of the slopes (a_1, $a_{2…}$) and the potential source fields (s_1, $s_{2…}$). Grid cell
299   fluxes are averaged over a geographical region to yield the average regional flux. We used the
300   standard deviation of the regression coefficients and the relative uncertainty in the surface
301   source, added in quadrature, to estimate the uncertainty in the flux (see Sect. 3.4.2 for fractional

302 uncertainties). We note that the uncertainty in STILT transport (see Sect. 2.3 for details) is
303 inherently reflected in the relative uncertainty of the regression coefficients (a_1, $a_{2...}$).

304 $$Z = aHs + b + \xi \tag{2}$$

305 $$Z = a_1Hs_1 + a_2Hs_2 + (a_3Hs_1Hs_2) ... + b + \xi \tag{3}$$

306

2.3.2 Surface Source Fields

308 Geophysical surface source fields of remotely sensed and reanalysis data included a combination
309 of sea ice concentration, chl a, absorption due to ocean detrital material, and downward
310 shortwave radiation at the ocean surface.

311 We used daily sea ice concentration data (https://nsidc.org/data/nsidc-0081) at a 25 km x 25 km
312 spatial resolution between 39.23° S and 90° S, 180° W – 180° E from the NASA National Snow
313 and Ice Data Center Distributed Active Archive Center (NSIDC; Maslanik et al., 1999). This
314 data reports the fraction of sea-ice cover, land-ice cover, and open water. Unfortunately, these
315 data do not provide any information on sea ice thickness, or the presence of brine channels or
316 melt ponds, which may modulate emissions from sea-ice covered regions. Sea ice concentration
317 data were calculated using measurements of near-real-time passive microwave brightness
318 temperature from the Special Sensor Microwave Image/Sounder (SSMIS) on the Defense
319 Meteorological Satellite Program (DMSP) satellites. NSIDC sea ice concentration data were
320 arithmetically averaged to yield 0.25° x 0.25° binned sea ice fraction for use with gridded surface
321 influences.

322 Due to persistent cloud cover over the Southern Ocean, which often precludes the retrieval of
323 remotely sensed ocean color data, we used 8-day mean composite Aqua MODIS L3 distributions
324 of chl a from the Ocean Color Index (OCI) algorithm and absorption due to gelbstoff and detrital
325 material at 443 nm from the Generalized Inherent Optical Properties (GIOP) model (NASA
326 Goddard Space Flight Center, 2014). Absorption due to gelbstoff and detrital material at 443 nm
327 is used as a proxy for colored dissolved organic matter (CDOM;
328 https://oceancolor.gsfc.nasa.gov/atbd/giop/). CDOM is hypothesized to be an important source of
329 carbon for the photochemical production of CH_3I (Moore et al., 1994). The GIOP model also
330 publishes an uncertainty in the absorption due to gelbstoff and detrital material at 443 nm. Raw
331 4 km x 4 km data were geometrically averaged, based on lognormal probability density
332 functions, to a spatial resolution of 0.25° x 0.25° for use with gridded surface influences. We
333 used the ratio of the 0.25° x 0.25° gridded uncertainty in the detrital material absorption to the
334 absorption as the relative uncertainty for flux calculations (see Sect. 3.4.2).

335 The National Center for Environmental Prediction (NCEP) provides Final Global Data
336 Assimilation System (GDAS/FNL) global data of downward shortwave radiation at the surface
337 at 0.25 degree and 6-hour resolution (NCEP, 2015). We chose downward shortwave radiation
338 for use with gridded surface influences because the photo-production of CH_3I has been observed
339 at all visible wavelengths (Moore et al., 1994). This reanalysis data is available at a higher

340 temporal resolution and better spatial coverage than satellite retrievals of photosynthetically
341 active radiation (PAR) or temperature.

342

343 **3 Results and discussion**

344 **3.1 Observed HVOC patterns and relationships**

345 Zonal cross-sections of HVOC data collected on ORCAS and ATom-2 illustrate unprecedented
346 spatial sampling across our study area between the surface and 12 km (Fig. 2). Above average
347 mixing ratios of CH_3I, $CHBr_3$, and $CHClBr_2$ typically remain confined to the lower ~2-4 km of
348 the atmosphere (Fig. 2a, b, d). These compounds have lifetimes of approximately two months or
349 less. Conversely, weak sources and longer lifetimes ($\geq$ 3 months) may have contributed to
350 similar concentrations of CH_2Br_2 and $CHBrCl_2$ throughout the troposphere and above average
351 mixing ratios as high as 8 km (Fig. 2c, e). Unfortunately, the availability of data above the
352 detection limit and absence of BL enhancements for $CHBrCl_2$ preclude the identification of
353 strong regional sources at this time. Meridional distributions also indicate lower latitude sources
354 of CH_3I and CH_3Br (< 50° S), potentially resulting from terrestrial and anthropogenic
355 contributions, and higher latitude sources (> 60° S) of $CHBr_3$, CH_2Br_2, and $CHClBr_2$ (Fig. 2a-
356 d,f).

357

358 **3.1.1 Observed HVOC interrelationships**

359 Across our study area in both 2016 and 2017, we found that $CHBr_3$ and CH_2Br_2 exhibit a
360 consistent enhancement ratio with each other in the bottom 2 km of the atmosphere both in
361 Region 1 and Region 2, which suggests that these bromocarbon fluxes are closely coupled.
362 Previous studies have documented co-located source regions of $CHBr_3$ and CH_2Br_2 in the
363 Southern Ocean (e.g. Hughes et al., 2009; Carpenter et al., 2000; Nightingale et al., 1995;
364 Laturnus et al., 1996), and laboratory studies have demonstrated that phytoplankton and their
365 associated bacteria cultures, including a cold water diatom isolated from coastal waters along the
366 Antarctic Peninsula and common to the Southern Ocean, produce both $CHBr_3$ and CH_2Br_2
367 (Hughes et al., 2013; Tokarczyk and Moore 1994; Sturges et al., 1993). The non-linearity
368 observed in ratios of these two gases at low $CHBr_3$ may reflect the different rates of their
369 production or loss in seawater, or possibly, the influence of air masses from distant, more
370 productive low-latitude source regions. Several studies have documented bacterially mediated
371 loss of CH_2Br_2, but not $CHBr_3$, and report distinct ratios of CH_2Br_2 to $CHBr_3$ in seawater during
372 the growth and senescent phases of a phytoplankton bloom (e.g. Carpenter et al., 2009, Hughes
373 et al., 2013). Although this analysis is restricted to the bottom 2 km of the atmosphere, zonal
374 transport of air masses with lower ratios of CH_2Br_2 to $CHBr_3$ ratios, as have been observed in the
375 MBL over productive, low-latitude regions, may also have influenced our observations
376 (Yokouchi et al. 2005). Mixing ratios of $CHBr_3$ and $CHClBr_2$ were also correlated (Fig. 3d) in
377 Region 2, and, a similar, weaker relationship was observed in Region 1 (Fig. 3b). $CHClBr_2$ is a

378   less well-studied compound than CH_2Br_2. Yet these consistent relationships suggest that $CHBr_3$
379   and $CHClBr_2$ may either share some of the same sources or have sources that co-vary.

380

381   **3.1.2 Observed HVOC relationships to $\delta(O_2/N_2)$ and CO_2**

382   We sought to test if the biologically mediated production of bromocarbons and oxygen result in
383   similar atmospheric distributions. Conversely, we expected HVOC atmospheric distributions
384   and CO_2 distributions to anticorrelate because CO_2 fixation in surface waters is proportional to
385   the production of oxygen.

386   For these comparisons, both O_2 and CO_2 mixing ratios from the upper troposphere (5-7 km) were
387   subtracted from the data to detrend for seasonal and inter-annual variability (Fig. 4; Fig. S3). To
388   isolate the contribution of ocean O_2 fluxes, the ORCAS $\delta(O_2/N_2)$ values reported here represent
389   the $\Delta\delta(O_2/N_2)$ to observed values between 5-7 km adjusted for CESM O_2 land and fossil fuel
390   contributions and the influence of air-sea N_2 fluxes. In Fig. 4 we present type II major axis
391   regression fits to data (fits were calculated using data scaled to their full range) between the
392   ocean surface and the lowest 7 km for bromocarbons with photochemical lifetimes of ≥ 1 month
393   and from the lowest 2 km for CH_3I with a photochemical lifetime of ~ 1 week. We used a type II
394   major axis regression model to balance the influences of uncorrelated processes and
395   measurement uncertainty in HVOCs (on the y-axis) and uncorrelated processes and measurement
396   uncertainty in O_2 and CO_2 (on the x-axis) on the regression slope (Ayers et al., 2001; Glover et
397   al., 2011). As noted by previous studies, simple least squares linear regressions fail to account
398   for uncertainties in predictor variables (e.g. Cantrell et al., 2008).

399   The robust correlations of $CHBr_3$ and CH_2Br_2 with $\delta(O_2/N_2)$, in both 2016 and 2017 and in
400   Region 1 and Region 2, provide support for a regional biogenic source of these two HVOCs (Fig.
401   4a, b and Fig. 4d, e). The air-sea exchange of O_2 during summer in the Southern Ocean is driven
402   by net community production (the excess of photosynthesis over respiration) in the surface
403   mixed layer, surface warming, and to a lesser extent ocean advection and mixing (e.g. Stephens
404   et al., 1998; Tortell and Long 2009; Tortell et al., 2014). Note that we adjust for influences on
405   the $\delta(O_2/N_2)$ from thermal N_2 fluxes (see Equation 1, Sect. 2.1.2 for details). Biological O_2
406   supersaturation in the surface mixed layer develops quickly in the first several days of a
407   phytoplankton bloom and diminishes as community respiration increases and air-sea gas
408   exchange equilibrates the surface layer with the atmosphere on a timescale of ~ 1 week. $CHBr_3$
409   and CH_2Br_2 are emitted from phytoplankton during the exponential growth phase (Hughes et al.,
410   2013), which often coincides with high net community production and the accumulation of O_2 in
411   surface waters. The bulk air-sea equilibration time for an excess of $CHBr_3$ and other HVOCs is
412   less than two weeks, although the photochemical loss of HVOCs will alter their ratio over time
413   (see Supplement for details on calculations of bulk sea air equilibration times).

414   Our observations suggest a biological source for $CHBr_3$ and CH_2Br_2 in both Region 1 and Region
415   2 (Fig. 4). Interestingly, the slope of the regression between $CHBr_3$ and O_2 appears distinct in
416   Region 1 and Region 2, but between CH_2Br_2 is the same. Molar enrichment ratios are 0.20 $\pm$
417   0.01, and 0.07 $\pm$ 0.004 pmol : mol for $CHBr_3$ and CH_2Br_2 to O_2 in Region 1, and 0.32 $\pm$ 0.02, and

418   0.07 ± 0.004 pmol : mol in Region 2. We observe a weaker relationship between CH_3I and
419    $CHClBr_2$ and O_2 in Region 1 (Fig. 4c, d), consistent with the existence of other, non-biological
420   sources of CH_3I in this region. Figure 4f illustrates a strong relationship between CH_3I and O_2,
421   as well as $CHClBr_2$ and O_2, in Region 2, however, which implies that the dominant sources of
422   CH_3I and $CHClBr_2$ emissions over the Patagonian Shelf are biological. The corresponding molar
423   enrichment ratios of CH_3I to O_2 and $CHClBr_2$ to O_2 in Region 2 are 0.38 ± 0.03 pmol : mol and
424   0.19 ± 0.04 pmol: mol, respectively.

425   In contrast to O_2, air-sea fluxes of CO_2 over the Southern Ocean during summer reflect the
426   balance of opposing thermal and biological drivers (e.g. Stephens et al., 1998; 2018). Ocean
427   buffering chemistry results in CO_2 equilibration across the air-sea interface on a timescale of
428   several months. ORCAS observations showed a depletion of CO_2 in the MBL, indicating that
429   uptake driven by net photosynthesis dominated over thermally driven outgassing during the
430   several months preceding the campaign (Stephens et al., 2018). $CHBr_3$ and CH_2Br_2 in the
431   lowest 7 km were negatively correlated with CO_2 in both years in Region 1 and Region 2 (Fig.
432   S3a, b, d, e). Interestingly, CH_3I was not correlated with CO_2 in Region 1, likely due to the long
433   air-sea equilibration timescale of CO_2 compared with a 9-day air-sea equilibration time and a ~7-
434   day photochemical lifetime for CH_3I. For longer lived species, correlations for HVOCs to CO_2
435   have similar r^2-values as those for HVOCs to $\delta(O_2/N_2)$, but model and climatological estimates
436   of Southern Ocean CO_2 fluxes are much less certain than for O_2 (Anav et al., 2015; Nevison et
437   al., 2016). As a result, we use modeled O_2 fluxes as the basis for our HVOC flux estimates (see
438   Sect. 3.4.1 for details).

439

440   **3.2 Model-observation comparisons**

441   The ORCAS dataset provides an exceptional opportunity to evaluate the CAM-Chem HVOC
442   emission scheme (Ordoñez et al., 2012) at high latitudes in the Southern Hemisphere. We
443   compared modeled HVOC constituents to corresponding observations along the ORCAS flight
444   track (Fig. 5; Fig. 6).   In these figures, we used type II major axis regression models to balance
445   the measurement uncertainty (on the y-axis) and the inherent, yet difficult to quantify
446   representativeness and errors in a global atmospheric chemistry model (on the x-axis). We note
447   that this comparison may favor constituents with longer photochemical lifetimes, when transport
448   and mixing dominate over source heterogeneity.

449   In Region 1 and Region 2, both the model and observations indicate that elevated mixing ratios
450   of CH_3I remain confined to the MBL (Fig. 5a and Fig. 6a), presumably due to its relatively short
451   photochemical lifetime. Modeled and observed CH_3I are poorly correlated in Region 1 ($r^2 =$
452   0.20; Fig. 5b) and better correlated in Region 2 ($r^2 = 0.70$; Fig. 6b). In both regions, the model
453   underpredicts CH_3I in the upper troposphere and lower stratosphere (UTLS), likely stemming
454   from the poleward transport of lower latitude air masses, where CAM-Chem also exhibits a
455   negative bias. Mixing ratio comparisons with CAM-Chem over the tropics (see Figure 10 in
456   Ordoñez et al., 2012) depict similar or larger discrepancies, and have been attributed to stronger
457   than anticipated convective cells in the tropics. We found strong correlations and agreement to

458   within a factor of ~2 between modeled and observed $CHBr_3$ and CH_2Br_2 (Fig. 5c-f and Fig. 6c-f).
459   Relatively long lifetimes ($\geq$ 1 month) in Region 1 likely enable vertical and zonal transport of
460    $CHBr_3$ and CH_2Br_2 to the mid and upper troposphere (Fig. 5c and e). The model was biased low
461   with respect to measurements of CH_3Br by ~25% in Region 1 and Region 2 (Fig. 5g-h and Fig.
462   6g-h), potentially as a result of an incorrect surface lower boundary condition. The model
463   underpredicted the mean vertical gradient in $CHClBr_2$, although it did a reasonable job of
464   representing the mean vertical gradient in $CHBrCl_2$, in both Region 1 and Region 2. In both
465   cases, however, the model failed to capture the spatial variability in both $CHClBr_2$ and $CHBrCl_2$
466   observations (Fig. 5i-l and Fig. 6i-l). Region 2 contains stronger sources of HVOCs than Region
467   1, which has been documented in numerous ship-based campaigns and archived in the
468   Halocarbons in the Ocean and Atmosphere database (HalOcAt; https://halocat.geomar.de/).
469   Region 2 also has much higher chl a (Fig. S4), supporting biogenic sources for these gases.

470

471   **3.3 Relationships between STILT surface influence functions and observations**

472   We used the STILT model to explore the relationships between observed mixing ratios and the
473   upstream surface influence functions (Equations 2-3) of sea ice, chl a, absorption due to detritus,
474   and downward shortwave radiation at the surface, which relate to various regional hypothesized
475   sources of HVOCs such as marine phytoplankton, phytoplankton in sea ice brines, and
476   decomposing organic matter in surface seawater (e.g. Moore and Zafiriou 1994; Moore et al.,
477   1996; Tokarczyk and Moore 1994; Sturges et al., 1992).

478

479   We found no positive relationships between upstream sea-ice influence and any measured
480   HVOC Region 1 (Fig. 7). We interpret this result to mean that increased summertime sea ice acts
481   either to reduce the production of HVOCs by blocking sunlight or as a physical barrier to oceanic
482   emissions of HVOCs from under-ice algae. Both of these mechanisms are also consistent with a
483   link between enhanced $CHBr_3$ and CH_2Br_2 emissions due to sea-ice retreat and surface sea-ice
484   melt water (Carpenter et al., 2007).

485   In other studies, it has also been proposed that sea ice could be an important source for $CHBr_3$
486   and other HVOCs, since high mixing ratios of $CHBr_3$ have been observed at the sea-ice and ice-
487   snow interface in the austral winter (Abrahamsson et al., 2018) and in under-ice algae in the
488   austral spring (Sturges et al., 1993). At present, CAM-Chem v1.2 with very short-lived halogen
489   chemistry does not include a regional flux of HVOCs over sea-ice covered waters in summer,
490   and our results do not indicate a need to include one. Our data, which were collected in January
491   and February, however, cannot assess the importance of sea ice as a source of HVOCs in other
492   seasons, such as winter or spring (Abrahamsson et al., 2018; Sturges et al., 1993). More field
493   campaigns are needed to further study the seasonality and regional strength of sea ice related
494   HVOC emissions.

495   We observed a statistically significant positive correlation between the surface influence function
496   of 8-day satellite composites of chl a concentration, which is widely used as a proxy for near-

497 surface phytoplankton biomass, and mixing ratios of $CHBr_3$ and CH_2Br_2 in Region 1 (Fig. 8a, b).
498 This finding corroborates previous findings from ship-borne field campaigns and laboratory
499 studies that have suggested a biogenic source for these two bromocarbons (e.g., Moore et al.,
500 1996; Hughes et al., 2013), and further substantiates the current CAM-Chem parameterization of
501 regional bromocarbon emissions using satellite retrievals of chl a in polar regions. CH_3Br
502 mixing ratios were not significantly correlated with chl a surface influence functions (Fig. 8c).
503 Although potentially suggesting that marine phytoplankton and microalgae were not a strong
504 regional source of CH_3Br during ORCAS, it is also possible that the relatively long lifetime of
505 CH_3Br precludes a definitive analysis of its origin based on chl a using 7-day back-trajectories.
506 Neither $CHClBr_2$ nor $CHBrCl_2$ were significantly correlated with chl a composite surface
507 influence functions (data not shown); however, more observations of these short-lived species in
508 the remote MBL are needed to substantiate this result.

509 Similar to Lai et al. (2011), we observed a significant correlation between mixing ratios of CH_3I
510 and total weekly upstream influence functions of 8-day chl a composites (Fig. 8d). Weaker
511 correlations were observed with upstream influence functions on shorter timescales than seven
512 days. We found that CH_3I, particularly in Region 1, was better explained by a multi-linear
513 regression with two predictors: 1) the influence function of downward shortwave radiation at the
514 surface (Fig. 9a) and 2) the absorption of light due to detrital material (Fig. 9b), yielding
515 improved agreement between predicted and observed CH_3I (Fig. 9c). Several previous studies
516 have correlated mixing ratios of CH_3I to satellite retrievals of PAR and surface ocean
517 temperature, revealing a link to solar radiation (e.g. Happell et al., 1996; Yokouchi et al., 2001).

518 Although certain species of phytoplankton are capable of producing CH_3I (e.g. Manley and de la
519 Cuesta 1997; Hughes et al., 2011), several studies also indicate a non-biological source for CH_3I
520 in the surface ocean. This non-biological source, though not fully understood, requires light, a
521 humic like substance at the surface ocean supplying a carbon source and methyl group, and
522 reactive iodine (Moore and Zarifou 1994; Richter and Wallace 2004). Thus far, two chemical
523 mechanisms have been proposed for the non-biological production of methyl iodide, one – a
524 radical recombination of a methyl group and iodine involving UV photolysis (e.g. Moore and
525 Zarifou 1994), and two, a substitution reaction involving the reduction of an oxidant, such as iron
526 III (e.g. Williams et al. 2007).

527

3.4 Flux estimation

3.4.1 O_2-based emission estimates

530 We present a novel approach that facilitates a basin-wide HVOC flux estimate using the robust
531 relationship between airborne observations of O_2 and HVOCs combined with modeled O_2 fluxes.
532 Unlike the existing CAM-Chem HVOC biogenic flux parameterization, this method does not
533 rely on weekly retrievals of chl a at high latitudes, which are often patchy. In addition, our study
534 indicates that $CHBr_3$, CH_2Br_2, and $CHClBr_2$ and CH_3I are better correlated with marine derived
535 O_2 than the upstream influence of chl a.

536 For $CHBr_3$, CH_2Br_2, and $CHClBr_2$ we construct ocean emission inventories for January and
537 February using a scaled version of gridded modeled air-sea O_2 fluxes and the slopes (i.e. molar
538 ratios) of linear correlations between $\delta(O_2/N_2)$ and HVOC mixing ratios (Fig. 10). O_2 fluxes
539 were obtained from simulations using a configuration of the CESM model nudged to reanalysis
540 temperatures and winds as described in Stephens et al. (2018). An earlier free running version of
541 CESM was one of the best evaluated for reproducing the seasonal cycle of $\delta(O_2/N_2)$ over the
542 Southern Ocean (Nevinson et al., 2015; 2016). To date, the north-south gradient in atmospheric
543 O_2 has not been well reproduced by any models (Resplandy et al., 2016). Vertical gradients in O_2
544 on ORCAS indicate that CESM overestimated gradients by 47% on average; accordingly, O_2
545 fluxes were adjusted downward by 47% to better match the observations. This is obviously a
546 very simple adjustment to the modeled fluxes, and the actual air-sea O_2 flux biases in CESM
547 likely have a great deal of spatial and temporal heterogeneity. We calculated an uncertainty for
548 the CESM flux using a second, independent estimate of O_2 fluxes based on dissolved O_2
549 measurements in surface seawater. The Garcia and Keeling (2001) climatology has much
550 smoother temporal and spatial patterns than CESM flux estimates but also results in
551 overestimated atmospheric O_2 spatial gradients. We calculate the relative uncertainty in O_2 flux
552 as the ratio of the mean absolute difference between gridded Garcia and Keeling values (2001;
553 also adjusted down by 51 % everywhere to better match ORCAS observations) to the CESM
554 model flux estimates in Regions 1 and 2 (adjusted down by 47% everywhere). These
555 disagreements were 7.3 % and 3.4 % for Regions 1 and 2, respectively. Based on the ratios of
556 HVOC to O_2 mixing ratios in bivariate least squares regressions and these adjusted O_2 fluxes, we
557 estimate mean emissions of $CHBr_3$ and CH_2Br_2 in Region 1 and Region 2. Relative uncertainty
558 in the slopes (i.e., the standard deviation of the slopes) from these regressions and the mean
559 relative uncertainties in regional O_2 fluxes were added in quadrature to yield uncertainties in
560 calculated HVOC emission rates.

561

562 Figure 10 shows the mean emissions for Jan. and Feb. of $CHBr_3$, CH_2Br_2, and $CHClBr_2$ in
563 Region 1 and Region 2. Mean regional emissions of $CHBr_3$ and CH_2Br_2 and $CHClBr_2$ are 91 ± 8,
564 31 ± 17, and 11 ± 4 pmol m^{-2} hr^{-1} in Region 1 and 329 ± 23, 69 ± 5, and 24 ± 5 pmol m^{-2} hr^{-1} in
565 Region 2 (Table 1). The mean flux of CH_3I in Region 2 is 392 ± 32 (Table 1). Table 1 also lists
566 the mean Jan. and Feb. CAM-Chem emissions from Region 1 and Region 2, as well as emissions
567 from several other observational and modeling Antarctic polar studies. Our estimates fall within
568 the range of these other studies, which span every month of the year and whose estimated fluxes
569 range from negative (i.e. from the atmosphere into the ocean) to 3500 pmol m^{-2} hr^{-1} $CHBr_3$ in a
570 coastal bay during its peak in primary production. CAM-Chem emissions for all species are
571 significantly lower than our observationally derived values in Region 1, with the exception of
572 CH_3I. Conversely, CAM-Chem emissions are significantly higher than our estimated emissions
573 in Region 2, with the exception of $CHClBr_2$ in Region 1, which remains underpredicted by the
574 model (Table 1). We note that in Region 2, CAM-Chem fluxes of $CHBr_3$ and CH_2Br_2, although
575 still significantly different, are more similar to our estimated fluxes.

576

3.4.2 STILT-based emission estimates

Similar to our O_2-based emission estimates, we used the relationship between surface influence functions and CH_3I mixing ratios (Fig. 9) to predict a flux field in Region 1 (Fig. 11). We used a multiple linear regression (± 1standard deviations; Equation 2), where Hs_1 and Hs_2 are the downward shortwave radiation and detrital absorption surface influence functions, respectively, with an intercept $b = 0.19 \pm 0.01$, and influence coefficients $a_1 = 3.7E\text{-}5 \pm 1.3E\text{-}5$, $a_2 = 3.5 \pm 0.74$, and an interaction term with the coefficient $a_3 = -5.2E\text{-}4 \pm 1.5E\text{-}4$ (Fig.9c). These regression coefficients and interaction term were used to estimate an average non-biological flux of CH_3I (Fig. 11; Table 1). This method could be used in place of the current Bell et al. (2002) climatology to update near weekly (~8 day) emissions of CH_3I in future versions of CAM-Chem. Our estimated mean CH_3I flux in Region 1 (35 ± 29 pmol m^{-2} hr^{-1}) is significantly lower than the current CAM-Chem estimated emissions (Table 1). As noted in Sect. 3.2, our observations of CH_3I are also much lower than the modeled mixing ratios. As discussed above, the strong correlations between CH_3I and O_2 in Region 2 also suggest a dominant biological source for this compound in this region. As a result, we have not used this relationship to parameterize a flux for CH_3I in Region 2 (see Sect. 3.1.2 and 3.4.1 for details). We note that although it would be possible to provide STILT-based emission estimates for other HVOCs (e.g. $CHBr_3$ and CH_2Br_2), the correlations these compounds were less strong with surface influence functions than those with O_2/N_2.

4 Conclusions

Our work combined TOGA and AWAS HVOC airborne observations from the ORCAS and ATom-2 campaigns, with coincident measurements of O_2 and CO_2, geophysical datasets and numerical models, including the global atmospheric chemistry model CAM-Chem, and the Lagrangian transport model, STILT. We evaluated model predictions, calculated molar enrichment ratios, inferred regional sources, and provided novel means of parameterizing ocean fluxes. We found that the Southern Ocean MBL is enriched in HVOCs, but that these MBL enhancements are less pronounced at higher latitudes, i.e., poleward of 60° S (Region 1) than over the productive Patagonian shelf (Region 2). Overall, our results indicated that the Southern Ocean is a moderate regional source of $CHBr_3$, CH_2Br_2, and CH_3I, and a weak source of $CHClBr_2$ and $CHBrCl_2$ in January and February. Good model-measurement correlations were obtained between our observations and simulations from the Community Earth System Model (CESM) atmospheric component with chemistry (CAM-Chem) for $CHBr_3$, CH_2Br_2, CH_3I, and $CHClBr_2$ but all showed significant differences in model:measurement ratios. The model:measurement comparison for CH_3Br was satisfactory and for $CHBrCl_2$ the low levels present precluded us from making a complete assessment.

$CHBr_3$ and CH_2Br_2 exhibited strong and robust correlations with each other and with O_2 and weaker but statistically significant correlations with the influence of chl a, which is a proxy for phytoplankton biomass. $CHClBr_2$ and $CHBr_3$ were well correlated with one another, particularly in Region 2. Together, these correlations suggested a biological source for these gases over the Southern Ocean. We found that CH_3I mixing ratios in Region 1 were best correlated with a non-

618 biological surface influence function, although biogenic CH_3I emissions appear important in
619 Region 2.

620

621 Our flux estimates based on the relationship of HVOC mixing ratios to O_2 and remotely sensed
622 parameters (for CH_3I) were compared with those derived from global models and ship-based
623 studies (Table 1). Our emission estimates of $CHBr_3$, CH_2Br_2, and $CHClBr_2$ are significantly
624 higher than CAM-Chem's globally prescribed emissions in Region 1, where HVOC mixing
625 ratios are under predicted (Table 1; Fig. 5). Similarly, our estimate of $CHClBr_2$ emissions is also
626 significantly higher than CAM-Chem's in Region 2, where $CHClBr_2$ mixing ratios remained
627 underpredicted. To the best of our knowledge, CAM-Chem's global parameterization of HVOC
628 fluxes has not been previously compared with data at high latitudes. Indeed, our emission
629 estimates of $CHBr_3$, CH_2Br_2, CH_3I fall within a range of CAM-Chem's esimtates (on the low
630 end) and most prior estimates based on either other models or localized studies using seawater-
631 side measurements from the Antarctic polar region in summer (on the high end). In the case of
632 CH_3I, our estimated emissions suggest that the prescribed emissions in CAM-Chem may be too
633 high in Region 1 and Region 2. Our parameterizations of the CH_3I flux could be used to explore
634 inter-annual variability in emissions, which is not captured by the Bell et al. (2002) CH_3I
635 climatology currently employed in CAM-Chem.

636 To extend these relationships to year-round and global parameterizations for use in global
637 climate models, they must be studied using airborne observations in other seasons and regions.
638 These approaches may help parameterize emissions of new species that can be correlated with
639 surface influence functions or the biological production of oxygen or may improve existing
640 emissions, where persistent biases exist. Finally, future airborne observations of HVOCs have
641 the potential to further improve our understanding of air-sea flux rates and their drivers for these
642 chemically and climatically important gases over the Southern Ocean.

643 *Data Availability*. The ORCAS and ATom-2 datasets are publically available at
644 https://doi.org/10.5065/D6SB445X ; (www.eol.ucar.edu/field_projects/orcas) and
645 https://doi.org/10.3334/ORNLDAAC/1581.

646 *Author Contributions*. EA is responsible for the bulk of the conceptualization, formal analysis,
647 writing, review, and editing with contributions from all authors. BBS and ECA were
648 instrumental in the investigation and supervision related to this manuscript. RSH contributed to
649 the conceptualization, as well as the investigation and HVOC data curation for this project. BBS,
650 EJM, and RFK were responsible for the data curation of $\delta(O_2/N_2)$ data and contributed to formal
651 analysis involving these data. MSHM along with EAK were responsible for STILT data curation
652 and formal analysis, and the conceptualization and formal analysis of SITLT-based geostatistical
653 influence functions and flux estimates were also informed by these two. DK, along with ST, JFL
654 and ASL were responsible for constructing CAM HVOC emissions and conducting CAM runs.
655 MCL was responsible for CESM simulations yielding O_2 fluxes and comparing this product
656 alongside the Garcia and Keeling O_2 climatology in CAM. KMC and CM were responsible for
657 the data curation of CO_2 observations. AJH contributed to the investigation for HVOC data.

658

671

References

Abrahamsson, K., Lorén, A., Wulff, A. and Wängberg, S.-Å.: Air–sea exchange of halocarbons: the influence of diurnal and regional variations and distribution of pigments, Deep Sea Research Part II: Topical Studies in Oceanography, 51(22-24), 2789–2805, doi:10.1016/j.dsr2.2004.09.005, 2004a.

Abrahamsson, K., Bertilsson, S., Chierici, M., Fransson, A., Froneman, P. W., Lorén, A. and Pakhomov, E. A.: Variations of biochemical parameters along a transect in the Southern Ocean, with special emphasis on volatile halogenated organic compounds, Deep Sea Research Part II: Topical Studies in Oceanography, 51(22-24), 2745–2756, doi:10.1016/j.dsr2.2004.09.004, 2004b.

Abrahamsson, K., Granfors, A., Ahnoff, M., Cuevas, C. A. and Saiz-Lopez, A.: Organic bromine compounds produced in sea ice in Antarctic winter, Nature Communications, 9(1), doi:10.1038/s41467-018-07062-8, 2018.

Anav, A., Friedlingstein, P., Beer, C., Ciais, P., Harper, A., Jones, C., Murray-Tortarolo, G., Papale, D., Parazoo, N. C., Peylin, P., Piao, S., Sitch, S., Viovy, N., Wiltshire, A. and Zhao, M.: Spatiotemporal patterns of terrestrial gross primary production: A review: GPP Spatiotemporal Patterns, Reviews of Geophysics, 53(3), 785–818, doi:10.1002/2015RG000483, 2015.

Apel, E.: ORCAS Trace Organic Gas Analyzer (TOGA) VOC Data. Version 1.0, [online] Available from: https://data.eol.ucar.edu/dataset/490.018 (Accessed 29 January 2019), 2017.

Apel, E. C., Hornbrook, R. S., Hills, A. J., Blake, N. J., Barth, M. C., Weinheimer, A., Cantrell, C., Rutledge, S. A., Basarab, B., Crawford, J., Diskin, G., Homeyer, C. R., Campos, T., Flocke, F., Fried, A., Blake, D. R., Brune, W., Pollack, I., Peischl, J., Ryerson, T., Wennberg, P. O., Crounse, J. D., Wisthaler, A., Mikoviny, T., Huey, G., Heikes, B., O'Sullivan, D. and Riemer, D. D.: Upper tropospheric ozone production from lightning NO_x -impacted convection: Smoke ingestion case study from the DC3 campaign, Journal of Geophysical Research: Atmospheres, 120(6), 2505–2523, doi:10.1002/2014JD022121, 2015.

Atkinson, H. M., Huang, R.-J., Chance, R., Roscoe, H. K., Hughes, C., Davison, B., Schönhardt, A., Mahajan, A. S., Saiz-Lopez, A., Hoffmann, T. and Liss, P. S.: Iodine emissions from the sea ice of the Weddell Sea, Atmospheric Chemistry and Physics, 12(22), 11229–11244, doi:10.5194/acp-12-11229-2012, 2012.

Atlas, E.: ORCAS Advanced Whole Air Sampler (AWAS) Data. Version 1.0, [online] Available from: https://data.eol.ucar.edu/dataset/490.027 (Accessed 29 January 2019), 2017.

Ayers, G. P.: Comment on regression analysis of air quality data, Atmospheric Environment, 35(13), 2423–2425, doi:10.1016/S1352-2310(00)00527-6, 2001.

Bates, T. S.: Preface [to special section on First Aerosol Characterization Experiment (AGE 1)], Journal of Geophysical Research: Atmospheres, 104(D17), 21645–21647, doi:10.1029/1999JD900365, 1999.

Bell, N., Hsu, L., Jacob, D. J., Schultz, M. G., Blake, D. R., Butler, J. H., King, D. B., Lobert, J. M. and Maier-Reimer, E.: Methyl iodide: Atmospheric budget and use as a tracer of marine convection in global models: GLOBAL ATMOSPHERIC METHYL IODIDE, Journal of Geophysical Research: Atmospheres, 107(D17), ACH 8–1–ACH 8–12, doi:10.1029/2001JD001151, 2002.

Blake, N. J., Blake, D. R., Wingenter, O. W., Sive, B. C., Kang, C. H., Thornton, D. C., Bandy, A. R., Atlas, E., Flocke, F., Harris, J. M. and Rowland, F. S.: Aircraft measurements of the latitudinal, vertical, and seasonal variations of NMHCs, methyl nitrate, methyl halides, and DMS during the First Aerosol Characterization Experiment (ACE 1), Journal of Geophysical Research: Atmospheres, 104(D17), 21803–21817, doi:10.1029/1999JD900238, 1999.

Blei, E. and Heal, M. R.: Methyl bromide and methyl chloride fluxes from temperate forest litter, Atmospheric Environment, 45(8), 1543–1547, doi:10.1016/j.atmosenv.2010.12.044, 2011.

Bloss, W. J., J. D. Lee, G. P. Johnson, R. Sommariva, D. E. Heard, A. Saiz-Lopez, J. M. C. Plane, G. McFiggans, M. Flynn, P. Williams, A. R. Rickard and Z. L. Fleming: Impact of halogen monoxide chemistry upon boundary layer OH and HO_2 concentrations at a coastal site, Geophysical Research Letters, 32(6), doi:10.1029/2004GL022084, 2005.

718

Boden, T., Andres, R. and Marland, G.: Global, Regional, and National Fossil-Fuel CO_2 Emissions (1751 - 2014) (V. 2017), [online] Available from: https://www.osti.gov/servlets/purl/1389331/ (Accessed 25 November 2018), 2017.

Boucher, O., Moulin, C., Belviso, S., Aumont, O., Bopp, L., Cosme, E., von Kuhlmann, R., Lawrence, M. G., Pham, M., Reddy, M. S., Sciare, J. and Venkataraman, C.: DMS atmospheric concentrations and sulphate aerosol indirect radiative forcing: a sensitivity study to the DMS source representation and oxidation, Atmospheric Chemistry and Physics, 3(1), 49–65, doi:10.5194/acp-3-49-2003, 2003.

Butler, J. H., King, D. B., Lobert, J. M., Montzka, S. A., Yvon-Lewis, S. A., Hall, B. D., Warwick, N. J., Mondeel, D. J., Aydin, M. and Elkins, J. W.: Oceanic distributions and emissions of short-lived halocarbons: OCEANIC EMISSIONS OF SHORT-LIVED HALOCARBONS, Global Biogeochemical Cycles, 21(1), doi:10.1029/2006GB002732, 2007.

Cantrell, C. A.: Technical Note: Review of methods for linear least-squares fitting of data and application to atmospheric chemistry problems, Atmospheric Chemistry and Physics, 8(17), 5477–5487, doi:10.5194/acp-8-5477-2008, 2008.

Carpenter, L. J., Liss, P. S. and Penkett, S. A.: Marine organohalogens in the atmosphere over the Atlantic and Southern Oceans: MARINE ORGANOHALOGENS IN THE ATMOSPHERE, Journal of Geophysical Research: Atmospheres, 108(D9), n/a–n/a, doi:10.1029/2002JD002769, 2003.

Carpenter, L. J., Wevill, D. J., Palmer, C. J. and Michels, J.: Depth profiles of volatile iodine and bromine-containing halocarbons in coastal Antarctic waters, Marine Chemistry, 103(3-4), 227–236, doi:10.1016/j.marchem.2006.08.003, 2007.

Carpenter, L. J., Jones, C. E., Dunk, R. M., Hornsby, K. E. and Woeltjen, J.: Air-sea fluxes of biogenic bromine from the tropical and North Atlantic Ocean, Atmospheric Chemistry and Physics, 9(5), 1805–1816, doi:10.5194/acp-9-1805-2009, 2009.

Chuck, A. L.: Oceanic distributions and air-sea fluxes of biogenic halocarbons in the open ocean, Journal of Geophysical Research, 110(C10), doi:10.1029/2004JC002741, 2005.

Colomb, A., Yassaa, N., Williams, J., Peeken, I. and Lochte, K.: Screening volatile organic compounds (VOCs) emissions from five marine phytoplankton species by head space gas chromatography/mass spectrometry (HS-GC/MS), Journal of Environmental Monitoring, 10(3), 325, doi:10.1039/b715312k, 2008.

Drewer, J., Heal, K. V., Smith, K. A. and Heal, M. R.: Methyl bromide emissions to the atmosphere from temperate woodland ecosystems, Global Change Biology, doi:10.1111/j.1365-2486.2008.01676.x, 2008.

Emmons, L. K., Walters, S., Hess, P. G., Lamarque, J.-F., Pfister, G. G., Fillmore, D., Granier, C., Guenther, A., Kinnison, D., Laepple, T., Orlando, J., Tie, X., Tyndall, G., Wiedinmyer, C., Baughcum, S. L. and Kloster, S.: Description and evaluation of the Model for Ozone and Related chemical Tracers, version 4 (MOZART-4), Geoscientific Model Development, 3(1), 43–67, doi:10.5194/gmd-3-43-2010, 2010.

Fernandez, R. P., Salawitch, R. J., Kinnison, D. E., Lamarque, J.-F. and Saiz-Lopez, A.: Bromine partitioning in the tropical tropopause layer: implications for stratospheric injection, Atmospheric Chemistry and Physics, 14(24), 13391–13410, doi:10.5194/acp-14-13391-2014, 2014.

Finlayson-Pitts, B. J.: The Tropospheric Chemistry of Sea Salt: A Molecular-Level View of the Chemistry of NaCl and NaBr, Chemical Reviews, 103(12), 4801–4822, doi:10.1021/cr020653t, 2003.

Garcia, H. E. and Keeling, R. F.: On the global oxygen anomaly and air-sea flux, Journal of Geophysical Research: Oceans, 106(C12), 31155–31166, doi:10.1029/1999JC000200, 2001.

Gent, P. R., Danabasoglu, G., Donner, L. J., Holland, M. M., Hunke, E. C., Jayne, S. R., Lawrence, D. M., Neale, R. B., Rasch, P. J., Vertenstein, M., Worley, P. H., Yang, Z.-L. and Zhang, M.: The Community Climate System Model Version 4, Journal of Climate, 24(19), 4973–4991, doi:10.1175/2011JCLI4083.1, 2011.

763 von Glasow, R. and Crutzen, P. J.: Model study of multiphase DMS oxidation with a focus on halogens,
764 Atmospheric Chemistry and Physics, 4(3), 589–608, doi:10.5194/acp-4-589-2004, 2004.

765 von Glasow, R., von Kuhlmann, R., Lawrence, M. G., Platt, U. and Crutzen, P. J.: Impact of reactive bromine
766 chemistry in the troposphere, Atmospheric Chemistry and Physics, 4(11/12), 2481–2497, doi:10.5194/acp-4-2481-
767 2004, 2004.

768 Glover, D. M., Jenkins, W. J. and Doney, S. C.: Modeling Methods for Marine Science, Cambridge University
769 Press., 2011.

770 Guenther, A. B., Jiang, X., Heald, C. L., Sakulyanontvittaya, T., Duhl, T., Emmons, L. K. and Wang, X.: The Model
771 of Emissions of Gases and Aerosols from Nature version 2.1 (MEGAN2.1): an extended and updated framework for
772 modeling biogenic emissions, Geoscientific Model Development, 5(6), 1471–1492, doi:10.5194/gmd-5-1471-2012,
773 2012.

774 Happell, J. D., Wallace, D. W. R., Wills, K. D., Wilke, R. J. and Neill, C. C.: A purge-and-trap capillary column gas
775 chromatographic method for the measurement of halocarbons in water and air. [online] Available from:
776 http://www.osti.gov/servlets/purl/366493-84sOfy/webviewable/ (Accessed 26 July 2018), 1996.

777 Hossaini, R., Mantle, H., Chipperfield, M. P., Montzka, S. A., Hamer, P., Ziska, F., Quack, B., Krüger, K.,
778 Tegtmeier, S., Atlas, E., Sala, S., Engel, A., Bönisch, H., Keber, T., Oram, D., Mills, G., Ordóñez, C., Saiz-Lopez,
779 A., Warwick, N., Liang, Q., Feng, W., Moore, F., Miller, B. R., Marécal, V., Richards, N. A. D., Dorf, M. and
780 Pfeilsticker, K.: Evaluating global emission inventories of biogenic bromocarbons, Atmospheric Chemistry and
781 Physics, 13(23), 11819–11838, doi:10.5194/acp-13-11819-2013, 2013.

782 Hughes, C., Chuck, A. L., Rossetti, H., Mann, P. J., Turner, S. M., Clarke, A., Chance, R. and Liss, P. S.: Seasonal
783 cycle of seawater bromoform and dibromomethane concentrations in a coastal bay on the western Antarctic
784 Peninsula: BROMOCARBON SEASONALITY ANTARCTICA, Global Biogeochemical Cycles, 23(2), n/a–n/a,
785 doi:10.1029/2008GB003268, 2009.

786 Hughes, C., Johnson, M., Utting, R., Turner, S., Malin, G., Clarke, A. and Liss, P. S.: Microbial control of
787 bromocarbon concentrations in coastal waters of the western Antarctic Peninsula, Marine Chemistry, 151, 35–46,
788 doi:10.1016/j.marchem.2013.01.007, 2013.

789 Hurrell, J. W., Hack, J. J., Shea, D., Caron, J. M. and Rosinski, J.: A New Sea Surface Temperature and Sea Ice
790 Boundary Dataset for the Community Atmosphere Model, Journal of Climate, 21(19), 5145–5153,
791 doi:10.1175/2008JCLI2292.1, 2008.

792 Keeling, R. F., Manning, A. C., McEvoy, E. M. and Shertz, S. R.: Methods for measuring changes in atmospheric O_2
793 concentration and their application in southern hemisphere air, Journal of Geophysical Research: Atmospheres,
794 103(D3), 3381–3397, doi:10.1029/97JD02537, 1998.

795 Lai, S. C., Williams, J., Arnold, S. R., Atlas, E. L., Gebhardt, S. and Hoffmann, T.: Iodine containing species in the
796 remote marine boundary layer: A link to oceanic phytoplankton: IODINE SPECIES AND PHYTOPLANKTON,
797 Geophysical Research Letters, 38(20), n/a–n/a, doi:10.1029/2011GL049035, 2011.

798 Lamarque, J.-F.: Response of a coupled chemistry-climate model to changes in aerosol emissions: Global impact on
799 the hydrological cycle and the tropospheric burdens of OH, ozone, and NO_x, Geophysical Research Letters, 32(16),
800 doi:10.1029/2005GL023419, 2005.

801 Lamarque, J.-F., Emmons, L. K., Hess, P. G., Kinnison, D. E., Tilmes, S., Vitt, F., Heald, C. L., Holland, E. A.,
802 Lauritzen, P. H., Neu, J., Orlando, J. J., Rasch, P. J. and Tyndall, G. K.: CAM-chem: description and evaluation of
803 interactive atmospheric chemistry in the Community Earth System Model, Geoscientific Model Development, 5(2),
804 369–411, doi:10.5194/gmd-5-369-2012, 2012.

805 Laturnus, F.: Volatile halocarbons released from Arctic macroalgae, Marine Chemistry, 55(3-4), 359–366,
806 doi:10.1016/S0304-4203(97)89401-7, 1996.

807 Liang, Q., Atlas, E., Blake, D., Dorf, M., Pfeilsticker, K. and Schauffler, S.: Convective transport of very short lived
808 bromocarbons to the stratosphere, Atmospheric Chemistry and Physics, 14(11), 5781–5792, doi:10.5194/acp-14-
809 5781-2014, 2014.

810 Lin, J. C.: A near-field tool for simulating the upstream influence of atmospheric observations: The Stochastic Time-
811 Inverted Lagrangian Transport (STILT) model, Journal of Geophysical Research, 108(D16), ACH 2–1–ACH 2–17,
812 doi:10.1029/2002JD003161, 2003.

813 Liu, X., Easter, R. C., Ghan, S. J., Zaveri, R., Rasch, P., Shi, X., Lamarque, J.-F., Gettelman, A., Morrison, H., Vitt,
814 F., Conley, A., Park, S., Neale, R., Hannay, C., Ekman, A. M. L., Hess, P., Mahowald, N., Collins, W., Iacono, M.
815 J., Bretherton, C. S., Flanner, M. G. and Mitchell, D.: Toward a minimal representation of aerosols in climate
816 models: description and evaluation in the Community Atmosphere Model CAM5, Geoscientific Model
817 Development, 5(3), 709–739, doi:10.5194/gmd-5-709-2012, 2012.

818 Manley, S. L. and Dastoor, M. N.: Methyl iodide (CH3I) production by kelp and associated microbes, Marine
819 Biology, 98(4), 477–482, doi:10.1007/BF00391538, 1988.

820 Maslanik, J.: Near-Real-Time DMSP SSM/I-SSMIS Daily Polar Gridded Sea Ice Concentrations, Version 1, 1999.

821 Mattson, E., Karlsson, A., Smith, W. O. and Abrahamsson, K.: The relationship between biophysical variables and
822 halocarbon distributions in the waters of the Amundsen and Ross Seas, Antarctica, Marine Chemistry, 140-141, 1–9,
823 doi:10.1016/j.marchem.2012.07.002, 2012.

824 Mattsson, E., Karlsson, A. and Abrahamsson, K.: Regional sinks of bromoform in the Southern Ocean: REGIONAL
825 SINKS OF CHBR $_3$ IN THE ANTARCTIC, Geophysical Research Letters, 40(15), 3991–3996,
826 doi:10.1002/grl.50783, 2013.

827 Moore, R. M. and Groszko, W.: Methyl iodide distribution in the ocean and fluxes to the atmosphere, Journal of
828 Geophysical Research: Oceans, 104(C5), 11163–11171, doi:10.1029/1998JC900073, 1999.

829 Moore, R. M. and Zafiriou, O. C.: Photochemical production of methyl iodide in seawater, Journal of Geophysical
830 Research, 99(D8), 16415, doi:10.1029/94JD00786, 1994.

831 Moore, R. M., Webb, M., Tokarczyk, R. and Wever, R.: Bromoperoxidase and iodoperoxidase enzymes and
832 production of halogenated methanes in marine diatom cultures, Journal of Geophysical Research: Oceans, 101(C9),
833 20899–20908, doi:10.1029/96JC01248, 1996.

834 Murphy, D. M., Froyd, K. D., Bian, H., Brock, C. A., Dibb, J. E., DiGangi, J. P., Diskin, G., Dollner, M., Kupc, A.,
835 Scheuer, E. M., Schill, G. P., Weinzierl, B., Williamson, C. J. and Yu, P.: The distribution of sea-salt aerosol in the
836 global troposphere, Atmospheric Chemistry and Physics Discussions, 1–27, doi:10.5194/acp-2018-1013, 2018.

837 NASA Goddard Space Flight Center, O. E. L.: SeaWiFS Ocean Color Data, 2014.

838 National Centers For Environmental Prediction/National Weather Service/NOAA/U.S. Department Of Commerce:
839 NCEP GDAS/FNL 0.25 Degree Global Tropospheric Analyses and Forecast Grids, 2015.

840 Navarro, M. A., Atlas, E. L., Saiz-Lopez, A., Rodriguez-Lloveras, X., Kinnison, D. E., Lamarque, J.-F., Tilmes, S.,
841 Filus, M., Harris, N. R. P., Meneguz, E., Ashfold, M. J., Manning, A. J., Cuevas, C. A., Schauffler, S. M. and
842 Donets, V.: Airborne measurements of organic bromine compounds in the Pacific tropical tropopause layer,
843 Proceedings of the National Academy of Sciences, 112(45), 13789–13793, doi:10.1073/pnas.1511463112, 2015.

844 Neale, R. B., Richter, J., Park, S., Lauritzen, P. H., Vavrus, S. J., Rasch, P. J. and Zhang, M.: The Mean Climate of
845 the Community Atmosphere Model (CAM4) in Forced SST and Fully Coupled Experiments, Journal of Climate,
846 26(14), 5150–5168, doi:10.1175/JCLI-D-12-00236.1, 2013.

847 Nevison, C. D., Manizza, M., Keeling, R. F., Kahru, M., Bopp, L., Dunne, J., Tiputra, J., Ilyina, T. and Mitchell, B.
848 G.: Evaluating the ocean biogeochemical components of Earth system models using atmospheric potential oxygen
849 and ocean color data, Biogeosciences, 12(1), 193–208, doi:10.5194/bg-12-193-2015, 2015.

850 Nevison, C. D., Manizza, M., Keeling, R. F., Stephens, B. B., Bent, J. D., Dunne, J., Ilyina, T., Long, M.,
851 Resplandy, L., Tjiputra, J. and Yukimoto, S.: Evaluating CMIP5 ocean biogeochemistry and Southern Ocean carbon

uptake using atmospheric potential oxygen: Present-day performance and future projection: CMIP5 APO AND SOUTHERN OCEAN CARBON FLUX, Geophysical Research Letters, 43(5), 2077–2085, doi:10.1002/2015GL067584, 2016.

Nightingale, P. D., Malin, G. and Liss, P. S.: Production of chloroform and other low molecular-weight halocarbons by some species of macroalgae, Limnology and Oceanography, 40(4), 680–689, doi:10.4319/lo.1995.40.4.0680, 1995.

Nightingale, P. D., Malin, G., Law, C. S., Watson, A. J., Liss, P. S., Liddicoat, M. I., Boutin, J. and Upstill-Goddard, R. C.: In situ evaluation of air-sea gas exchange parameterizations using novel conservative and volatile tracers, Global Biogeochemical Cycles, 14(1), 373–387, 2000.

Obrist, D., Tas, E., Peleg, M., Matveev, V., Faïn, X., Asaf, D. and Luria, M.: Bromine-induced oxidation of mercury in the mid-latitude atmosphere, Nature Geoscience, 4, 22, 2010.

Ordóñez, C., Lamarque, J.-F., Tilmes, S., Kinnison, D. E., Atlas, E. L., Blake, D. R., Sousa Santos, G., Brasseur, G. and Saiz-Lopez, A.: Bromine and iodine chemistry in a global chemistry-climate model: description and evaluation of very short-lived oceanic sources, Atmospheric Chemistry and Physics, 12(3), 1423–1447, doi:10.5194/acp-12-1423-2012, 2012.

Quack, B. and Wallace, D. W. R.: Air-sea flux of bromoform: Controls, rates, and implications: AIR-SEA FLUX OF BROMOFORM, Global Biogeochemical Cycles, 17(1), doi:10.1029/2002GB001890, 2003.

Raimund, S., Quack, B., Bozec, Y., Vernet, M., Rossi, V., Garçon, V., Morel, Y. and Morin, P.: Sources of short-lived bromocarbons in the Iberian upwelling system, Biogeosciences, 8(6), 1551–1564, doi:10.5194/bg-8-1551-2011, 2011.

Read, K. A., Mahajan, A. S., Carpenter, L. J., Evans, M. J., Faria, B. V. E., Heard, D. E., Hopkins, J. R., Lee, J. D., Moller, S. J., Lewis, A. C., Mendes, L., McQuaid, J. B., Oetjen, H., Saiz-Lopez, A., Pilling, M. J. and Plane, J. M. C.: Extensive halogen-mediated ozone destruction over the tropical Atlantic Ocean, Nature, 453(7199), 1232–1235, doi:10.1038/nature07035, 2008.

Resplandy, L., Keeling, R. F., Stephens, B. B., Bent, J. D., Jacobson, A., Rödenbeck, C. and Khatiwala, S.: Constraints on oceanic meridional heat transport from combined measurements of oxygen and carbon, Climate Dynamics, 47(9-10), 3335–3357, doi:10.1007/s00382-016-3029-3, 2016.

Reygondeau, G., Longhurst, A., Martinez, E., Beaugrand, G., Antoine, D. and Maury, O.: Dynamic biogeochemical provinces in the global ocean: DYNAMIC BIOGEOCHEMICAL PROVINCES, Global Biogeochemical Cycles, 27(4), 1046–1058, doi:10.1002/gbc.20089, 2013.

Richter, U. and Wallace, D. W. R.: Production of methyl iodide in the tropical Atlantic Ocean: PRODUCTION OF METHYL IODIDE, Geophysical Research Letters, 31(23), doi:10.1029/2004GL020779, 2004.

Rienecker, M. M., Suarez, M. J., Todling, R., Bacmeister, J., Takacs, L., Liu, H. C., Gu, W., Sienkiewicz, M., Koster, R. D., Gelaro, R., Stajner, I. and Nielsen, J. E.: The GEOS-5 Data Assimilation System – Documentation of Versions 5.0.1, 5.1.0, and 5.2.0, NASA/TM-2008-104606., 2008.

Saiz-Lopez, A., Mahajan, A. S., Salmon, R. A., Bauguitte, S. J.-B., Jones, A. E., Roscoe, H. K. and Plane, J. M. C.: Boundary Layer Halogens in Coastal Antarctica, Science, 317(5836), 348–351, doi:10.1126/science.1141408, 2007.

Saiz-Lopez, A., Lamarque, J.-F., Kinnison, D. E., Tilmes, S., Ordóñez, C., Orlando, J. J., Conley, A. J., Plane, J. M. C., Mahajan, A. S., Sousa Santos, G., Atlas, E. L., Blake, D. R., Sander, S. P., Schauffler, S., Thompson, A. M. and Brasseur, G.: Estimating the climate significance of halogen-driven ozone loss in the tropical marine troposphere, Atmospheric Chemistry and Physics, 12(9), 3939–3949, doi:10.5194/acp-12-3939-2012, 2012.

Saiz-Lopez, A., Fernandez, R. P., Ordóñez, C., Kinnison, D. E., Gómez Martín, J. C., Lamarque, J.-F. and Tilmes, S.: Iodine chemistry in the troposphere and its effect on ozone, Atmospheric Chemistry and Physics, 14(23), 13119–13143, doi:10.5194/acp-14-13119-2014, 2014.

896   Salawitch, R. J., Canty, T., Kurosu, T., Chance, K., Liang, Q., da Silva, A., Pawson, S., Nielsen, J. E., Rodriguez, J.
897   M., Bhartia, P. K., Liu, X., Huey, L. G., Liao, J., Stickel, R. E., Tanner, D. J., Dibb, J. E., Simpson, W. R.,
898   Donohoue, D., Weinheimer, A., Flocke, F., Knapp, D., Montzka, D., Neuman, J. A., Nowak, J. B., Ryerson, T. B.,
899   Oltmans, S., Blake, D. R., Atlas, E. L., Kinnison, D. E., Tilmes, S., Pan, L. L., Hendrick, F., Van Roozendael, M.,
900   Kreher, K., Johnston, P. V., Gao, R. S., Johnson, B., Bui, T. P., Chen, G., Pierce, R. B., Crawford, J. H. and Jacob,
901   D. J.: A new interpretation of total column BrO during Arctic spring: FRONTIER, Geophysical Research Letters,
902   37(21), n/a–n/a, doi:10.1029/2010GL043798, 2010.

903   Schauffler, S. M., Atlas, E. L., Blake, D. R., Flocke, F., Lueb, R. A., Lee-Taylor, J. M., Stroud, V. and Travnicek,
904   W.: Distributions of brominated organic compounds in the troposphere and lower stratosphere, Journal of
905   Geophysical Research: Atmospheres, 104(D17), 21513–21535, doi:10.1029/1999JD900197, 1999.

906   Schroeder, W. H., Anlauf, K. G., Barrie, L. A., Lu, J. Y., Steffen, A., Schneeberger, D. R. and Berg, T.: Arctic
907   springtime depletion of mercury, Nature, 394, 331, 1998.

908   Simpson, W. R., Brown, S. S., Saiz-Lopez, A., Thornton, J. A. and von Glasow, R.: Tropospheric Halogen
909   Chemistry: Sources, Cycling, and Impacts, Chemical Reviews, 115(10), 4035–4062, doi:10.1021/cr5006638, 2015.

910   Sive, B. C., Varner, R. K., Mao, H., Blake, D. R., Wingenter, O. W. and Talbot, R.: A large terrestrial source of
911   methyl iodide, Geophysical Research Letters, 34(17), doi:10.1029/2007GL030528, 2007.

912   Stephens, B.: ORCAS Merge Products. Version 1.0, [online] Available from:
913   https://data.eol.ucar.edu/dataset/490.024 (Accessed 31 December 2018), 2017.

914   Stephens, B. B., Keeling, R. F., Heimann, M., Six, K. D., Murnane, R. and Caldeira, K.: Testing global ocean
915   carbon cycle models using measurements of atmospheric O_2 and CO_2 concentration, Global Biogeochemical
916   Cycles, 12(2), 213–230, doi:10.1029/97GB03500, 1998.

917   Stephens, B. B., Keeling, R. F. and Paplawsky, W. J.: Shipboard measurements of atmospheric oxygen using a
918   vacuum-ultraviolet absorption technique, Tellus B, 55(4), 857–878, doi:10.1046/j.1435-6935.2003.00075.x, 2003.

919   Stephens, B. B., Long, M. C., Keeling, R. F., Kort, E. A., Sweeney, C., Apel, E. C., Atlas, E. L., Beaton, S., Bent, J.
920   D., Blake, N. J., Bresch, J. F., Casey, J., Daube, B. C., Diao, M., Diaz, E., Dierssen, H., Donets, V., Gao, B.-C.,
921   Gierach, M., Green, R., Haag, J., Hayman, M., Hills, A. J., Hoecker-Martínez, M. S., Honomichl, S. B., Hornbrook,
922   R. S., Jensen, J. B., Li, R.-R., McCubbin, I., McKain, K., Morgan, E. J., Nolte, S., Powers, J. G., Rainwater, B.,
923   Randolph, K., Reeves, M., Schauffler, S. M., Smith, K., Smith, M., Stith, J., Stossmeister, G., Toohey, D. W. and
924   Watt, A. S.: The O_2/N_2 Ratio and CO_2 Airborne Southern Ocean Study, Bulletin of the American Meteorological
925   Society, 99(2), 381–402, doi:10.1175/BAMS-D-16-0206.1, 2018.

926   Sturges, W. T., Cota, G. F. and Buckley, P. T.: Bromoform emission from Arctic ice algae, Nature, 358, 660, 1992.

927   Sturges, W. T., Cota, G. F. and Buckley, P. T.: Vertical profiles of bromoform in snow, sea ice, and seawater in the
928   Canadian Arctic, Journal of Geophysical Research: Oceans, 102(C11), 25073–25083, doi:10.1029/97JC01860,
929   1997.

930   Tilmes, S., Lamarque, J.-F., Emmons, L. K., Kinnison, D. E., Marsh, D., Garcia, R. R., Smith, A. K., Neely, R. R.,
931   Conley, A., Vitt, F., Val Martin, M., Tanimoto, H., Simpson, I., Blake, D. R. and Blake, N.: Representation of the
932   Community Earth System Model (CESM1) CAM4-chem within the Chemistry-Climate Model Initiative (CCMI),
933   Geoscientific Model Development, 9(5), 1853–1890, doi:10.5194/gmd-9-1853-2016, 2016.

934   Tohjima, Y.: Preparation of gravimetric standards for measurements of atmospheric oxygen and reevaluation of
935   atmospheric oxygen concentration, Journal of Geophysical Research, 110(D11), doi:10.1029/2004JD005595, 2005.

936   Tokarczyk, R. and Moore, R. M.: Production of volatile organohalogens by phytoplankton cultures, Geophysical
937   Research Letters, 21(4), 285–288, doi:10.1029/94GL00009, 1994.

938   Tortell, P. D. and Long, M. C.: Spatial and temporal variability of biogenic gases during the Southern Ocean spring
939   bloom, Geophysical Research Letters, 36(1), doi:10.1029/2008GL035819, 2009.

940 Tortell, P. D., Asher, E. C., Ducklow, H. W., Goldman, J. A. L., Dacey, J. W. H., Grzymski, J. J., Young, J. N.,
941 Kranz, S. A., Bernard, K. S. and Morel, F. M. M.: Metabolic balance of coastal Antarctic waters revealed by
942 autonomous p CO $_2$ and ΔO $_2$ /Ar measurements: metabolic balance of Antarctic waters, Geophysical Research
943 Letters, 41(19), 6803–6810, doi:10.1002/2014GL061266, 2014.

944 Williams, J., Gros, V., Atlas, E., Maciejczyk, K., Batsaikhan, A., Schöler, H. F., Forster, C., Quack, B., Yassaa, N.,
945 Sander, R. and Van Dingenen, R.: Possible evidence for a connection between methyl iodide emissions and Saharan
946 dust, Journal of Geophysical Research, 112(D7), doi:10.1029/2005JD006702, 2007.

947 WMO (World Meteorological Organization): Scientific Assessment of Ozone Depletion: 2018, Global Ozone
948 Research and Monitoring Project-Report, Geneva, Switzerland., 2018.

949 Wofsy, S. C.: HIAPER Pole-to-Pole Observations (HIPPO): fine-grained, global-scale measurements of climatically
950 important atmospheric gases and aerosols, Philosophical Transactions of the Royal Society A: Mathematical,
951 Physical and Engineering Sciences, 369(1943), 2073–2086, doi:10.1098/rsta.2010.0313, 2011.

952 Wofsy, S. C., Afshar, S., Allen, H. M., Apel, E., Asher, E. C., Barletta, B., Bent, J., Bian, H., Biggs, B. C., Blake, D.
953 R., Blake, N., Bourgois, I., Brock, C. A., Brune, W. H., Budney, J. W., Bui, T. P., Butler, A., Campuzano-Jost, P.,
954 Chang, C. S., Chin, M., Commane, R., Correa, G., Crounse, J. D., Cullis, P. D., Daube, B. C., Day, D. A., Dean-
955 Day, J. M., Dibb, J. E., Digangi, J. P., Diskin, G. S., Dollner, M., Elkins, J. W., Erdesz, F., Fiore, A. M., Flynn, C.
956 M., Froyd, K., Gesler, D. W., Hall, S. R., Hanisco, T. F., Hannun, R. A., Hills, A. J., Hintsa, E. J., Hoffmann, A.,
957 Hornbrook, R. S., Huey, L. G., Hughes, S., Jimenez, J. L., Johnson, B. J., Katich, J. M., Keeling, R., Kim, M. J.,
958 Kupc, A., Lait, L. R., Lamarque, J.-F., Liu, H. B., McKain, K., Mclaughlin, R. J., Meinardi, S., Miller, D. O.,
959 Montzka, S. A., Moore, F. L., Morgan, E. J., Murphy, D. M., Murray, L. T., Nault, B. A., Neuman, J. A., Newman,
960 P. A., Nicely, J. M., Pan, X., Paplawsky, W., Peischl, J., Prather, M. J., Price, D. J., Ray, E., Reeves, J. M.,
961 Richardson, M., Rollins, A. W., Rosenlof, K. H., Ryerson, T. B., Scheuer, E., Schill, G. P., Schroder, J. C., Schwarz,
962 J. P., St.Clair, J. M., Steenrod, S. D., Stephens, B. B., Strode, S. A., Sweeney, C., Tanner, D., Teng, A. P., Thames,
963 A. B., Thompson, C. R., Ullmann, K., Veres, P. R., Vizenor, N., Wagner, N. L., Watt, A., Weber, R., Weinzierl, B.,
964 et al.: ATom: Merged Atmospheric Chemistry, Trace Gases, and Aerosols, [online] Available from:
965 https://daac.ornl.gov/cgi-bin/dsviewer.pl?ds_id=1581 (Accessed 31 December 2018), 2018.

966 Xiang, B., Miller, S. M., Kort, E. A., Santoni, G. W., Daube, B. C., Commane, R., Angevine, W. M., Ryerson, T. B.,
967 Trainer, M. K., Andrews, A. E., Nehrkorn, T., Tian, H. and Wofsy, S. C.: Nitrous oxide (N $_2$ O) emissions from
968 California based on 2010 CalNex airborne measurements: California N $_2$ O emissions, Journal of Geophysical
969 Research: Atmospheres, 118(7), 2809–2820, doi:10.1002/jgrd.50189, 2013.

970 Yang, B., Yang, G.-P., Lu, X.-L., Li, L. and He, Z.: Distributions and sources of volatile chlorocarbons and
971 bromocarbons in the Yellow Sea and East China Sea, Marine Pollution Bulletin, 95(1), 491–502,
972 doi:10.1016/j.marpolbul.2015.03.009, 2015.

973 Yokouchi, Y., Nojiri, Y., Barrie, L. A., Toom-Sauntry, D. and Fujinuma, Y.: Atmospheric methyl iodide: High
974 correlation with surface seawater temperature and its implications on the sea-to-air flux, Journal of Geophysical
975 Research: Atmospheres, 106(D12), 12661–12668, doi:10.1029/2001JD900083, 2001.

976 Yokouchi, Y., Hasebe, F., Fujiwara, M., Takashima, H., Shiotani, M., Nishi, N., Kanaya, Y., Hashimoto, S., Fraser,
977 P., Toom-Sauntry, D., Mukai, H. and Nojiri, Y.: Correlations and emission ratios among bromoform,
978 dibromochloromethane, and dibromomethane in the atmosphere, Journal of Geophysical Research, 110(D23),
979 doi:10.1029/2005JD006303, 2005.

980 Ziska, F., Quack, B., Abrahamsson, K., Archer, S. D., Atlas, E., Bell, T., Butler, J. H., Carpenter, L. J., Jones, C. E.,
981 Harris, N. R. P., Hepach, H., Heumann, K. G., Hughes, C., Kuss, J., Krüger, K., Liss, P., Moore, R. M., Orlikowska,
982 A., Raimund, S., Reeves, C. E., Reifenhäuser, W., Robinson, A. D., Schall, C., Tanhua, T., Tegtmeier, S., Turner,
983 S., Wang, L., Wallace, D., Williams, J., Yamamoto, H., Yvon-Lewis, S. and Yokouchi, Y.: Global sea-to-air flux
984 climatology for bromoform, dibromomethane and methyl iodide, Atmospheric Chemistry and Physics, 13(17),
985 8915–8934, doi:10.5194/acp-13-8915-2013, 2013.

986

987

988 **Tables**

989 Table 1. Mean ± uncertainty (see Sect. 3.4.1 and 3.4.2 for details) HVOC emission estimates
990 (pmol m^{-2} hr^{-1}) in Region 1 and Region 2 calculated in this study (with method indicated below
991 each value), from CAM-Chem (Ordoñez et al., 2012) and from several other modeling and ship-
992 based observational studies.

993

Region/Months	CHBr$_3$	CH$_2$Br$_2$	CH$_3$I	CHClBr$_2$	Reference
Region 1 (JF) < 60° S	91 ± 8 O$_2$ Regr.	31 ± 18 O$_2$ Regr.	35 ± 29 MLR	11 ± 4 O$_2$ Regr.	This Study
Region 2 (JF) >55° S and <40° S	329 ± 23 O$_2$ Regr.	69 ± 5 O$_2$ Regr.	392 ±32 O$_2$ Regr.	25 ± 5 O$_2$ Regr.	This Study
Region 1 (JF)	10	1.9	120	0.38	CAM-Chem
Region 2 (JF)	360	44	800	8.7	CAM-Chem
Southern Ocean (≥50°S), (DJ)	200	200	200	--------------	Ziska et al. 2013 (model)
Marguerite Bay (DJF)	3500	875	--------------	--------------	Hughes et al. 2009 (obs)
70°S-72°S Antarctica	1300	--------------	--------------	--------------	Carpenter et al. 2007 (obs)
Southern Ocean (≥50°S) (Feb. - April)	225	312	708	--------------	Butler et al. 2007 (obs)
40°S-52°S S. Atlantic (Sept.-Feb.)	-1670	--------------	250	--------------	Chuck et al. 2005
Southern Ocean (≥50°S), (DJ)	-330	--------------	--------------	--------------	Mattson et al. 2013 (model)

994

995

996

997 **Figures**
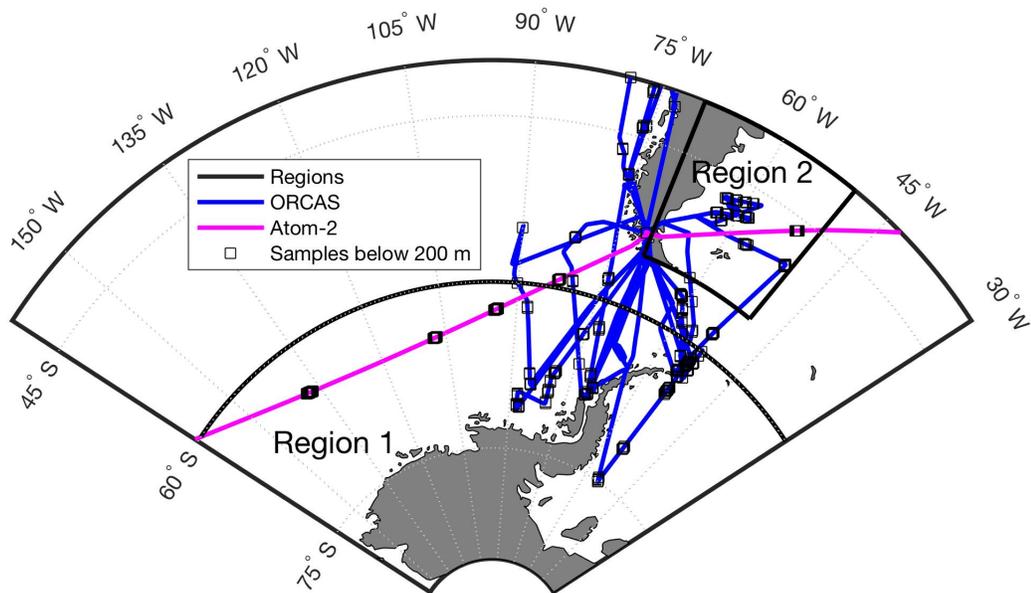
998

999 **Figure 1.** Overview map ORCAS and ATom-2 flight tracks in the study regions: 1) high
1000 latitudes in the Southern Hemisphere poleward 60° S and 2) the Patagonian Shelf. The ORCAS
1001 and ATom-2 aircraft flights and dips below 200 m that took place within these regions are also
1002 shown.

1003

1004
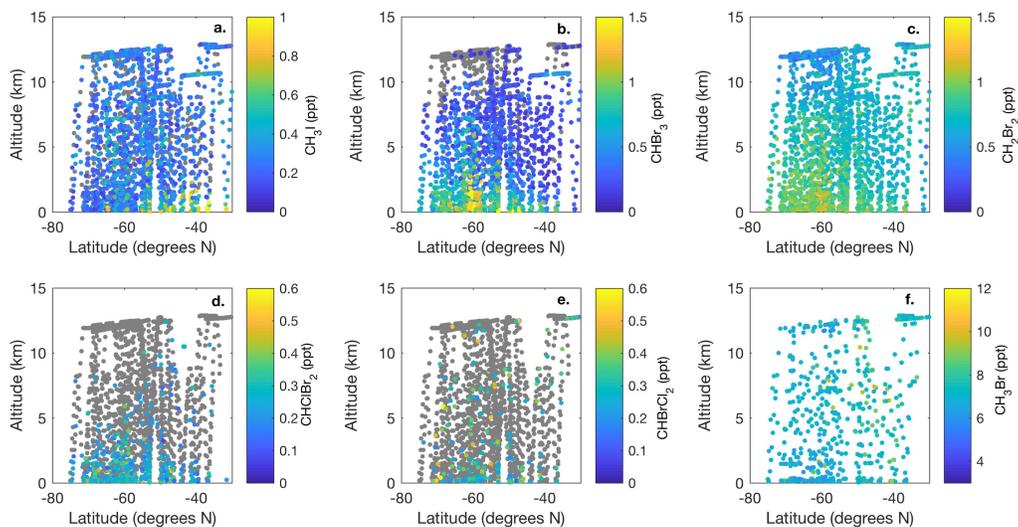
Figure 2. Meridional-altitudinal cross-sections of mixing ratios of a) CH_3I , b) $CHBr_3$, c) CH_2Br_2, d) $CHClBr_2$, and e) $CHBrCl_2$ from the TOGA and mixing ratios of f) CH_3Br from AWAS and WAS in 2016 and 2017, respectively, during the ORCAS and ATom-2 campaigns over the Southern Ocean in the austral summer. Note the different color bar scales. Gray points denote measurements below the detection limit of each species (CH_3I - 0.03 ppt, $CHBr_3$ – 0.2 ppt, CH_2Br_2 – 0.03 ppt, $CHClBr_2$ – 0.03 ppt, $CHBrCl_2$ – 0.05 ppt, CH_3Br – 0.2 ppt).
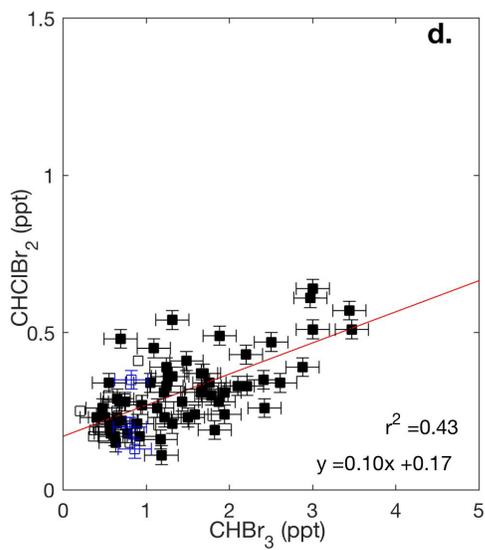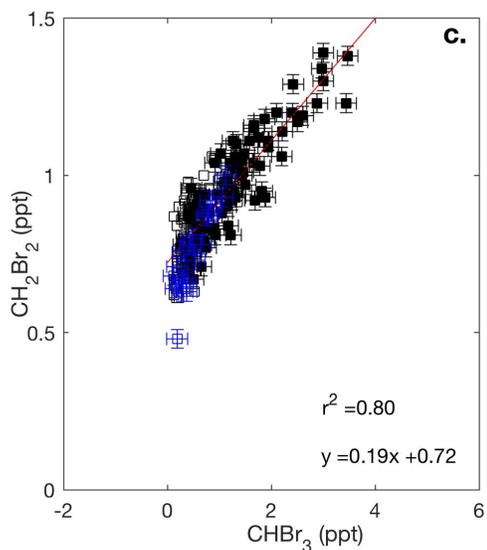
1013
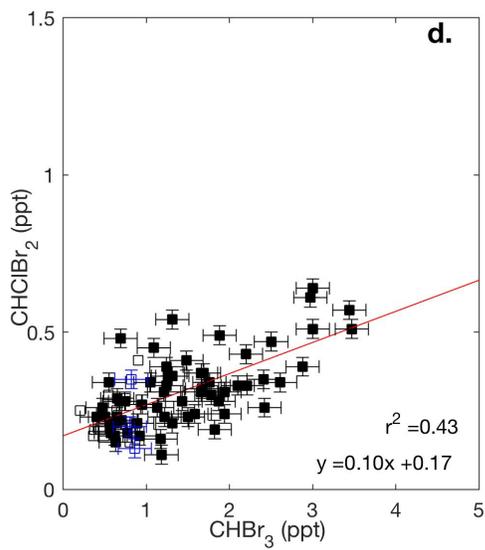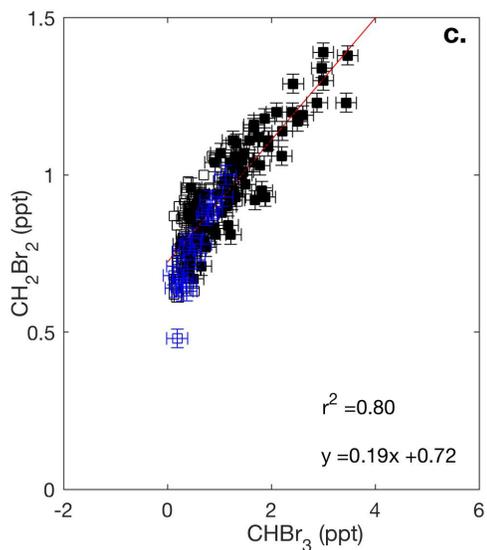
1014

1015

1016

Figure 3. Mixing ratios of $CHBr_3$ vs. CH_2Br_2 and $CHClBr_2$ across the ORCAS and ATom-2 campaigns in Region 1 (Fig.3a,b) and in (Fig.3c,d), respectively. Type II major axis regression model (bivariate least squares regressions) are based on ORCAS data below 2 km and illustrate regional enhancement ratios. Error bars represent the uncertainty in HVOC measurements.

1021

1022

1023

1024
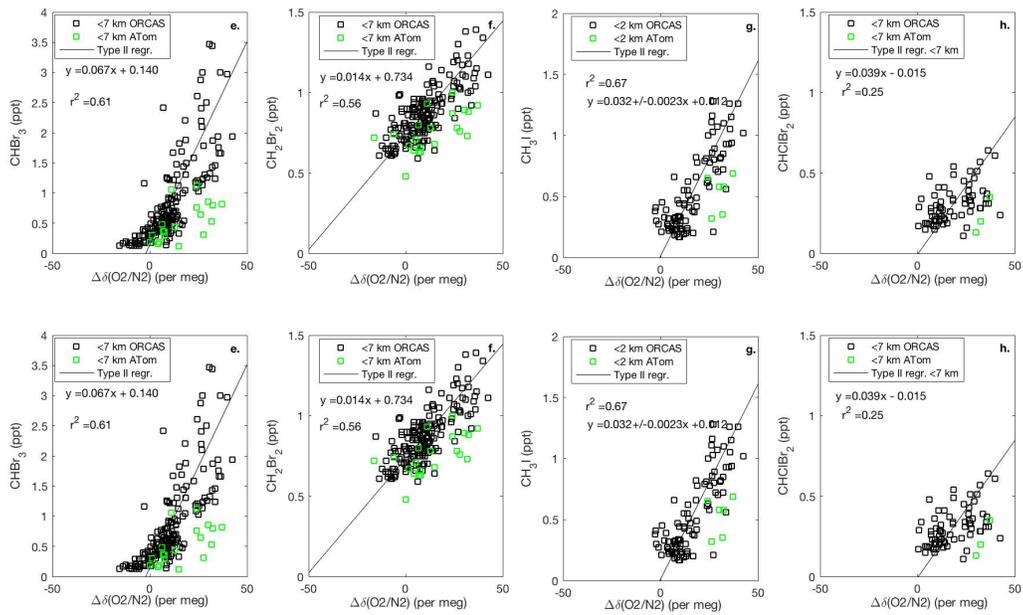
1025

1026

1027

Figure 4. Mixing ratios of $CHBr_3$, CH_2Br_2, and CH_3I vs. O_2 on ORCAS and ATom-2 in Region 1, poleward of 60° S (a-d) and Region 2 over the Patagonian Shelf (e-h). Slopes ± standard errors from type II major axis regression model (bivariate least squares regression) fits of ORCAS data for regressions with $r^2 > 0.2$ (fits were calculated on variables scaled to their full range). The slopes reported in the figure are converted to pmol:mol ratios prior to estimating biogenic HVOC fluxes based on modeled CESM O_2 fluxes. Data from above 7 km were excluded due to the influence of air masses transported from further north.

1035
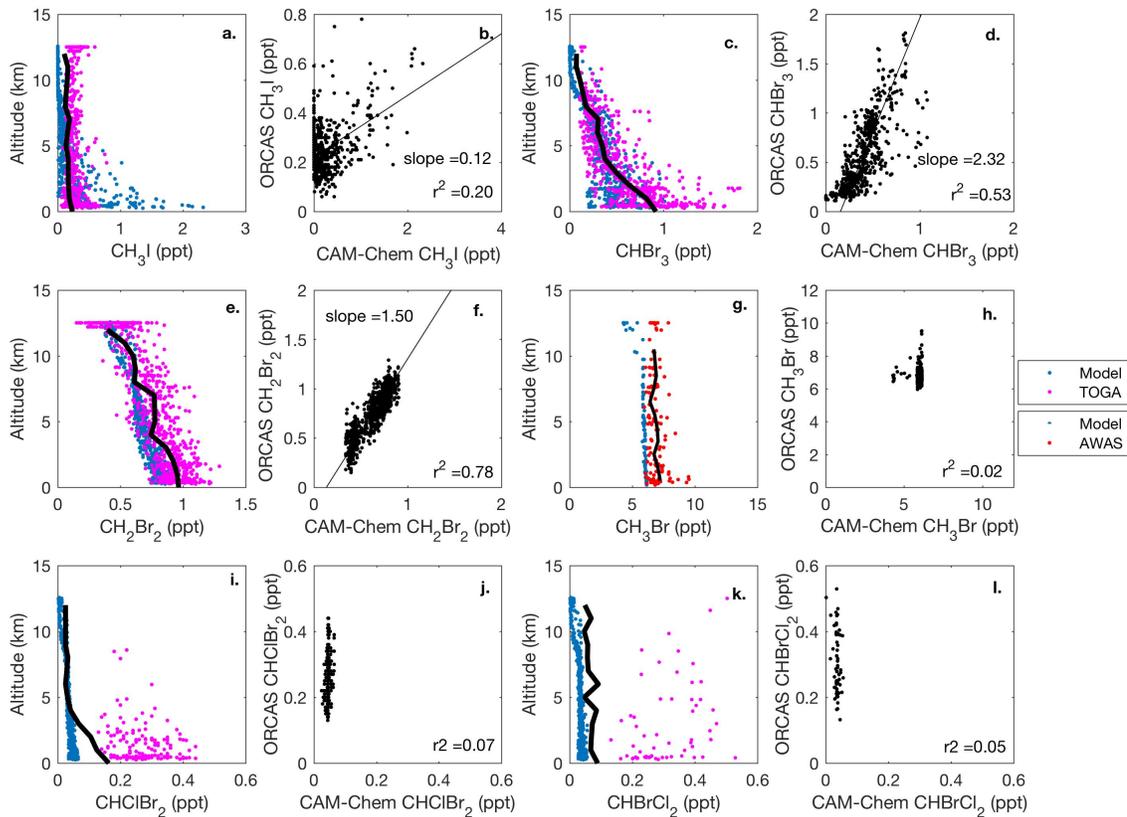
Fig 5. CAM-Chem1.2 model-aircraft measurement comparison during the ORCAS campaign between 1-12 km in Region 1, high latitudes in the Southern Hemisphere poleward 60° S. All regressions are type II major axis regression models bivariate least squares regressions (slopes are shown when the $r^2 \geq 0.2$). The bold, black line in each vertical profile represents the binned (mean) mixing ratio of HVOC measurements at that altitude. The binned mean includes measurements below the detection limit (DL), which for this calculation are assigned a value equal to the DL multiplied by the percentage of data below detection. Modeled values include locations where observations were below the DL.
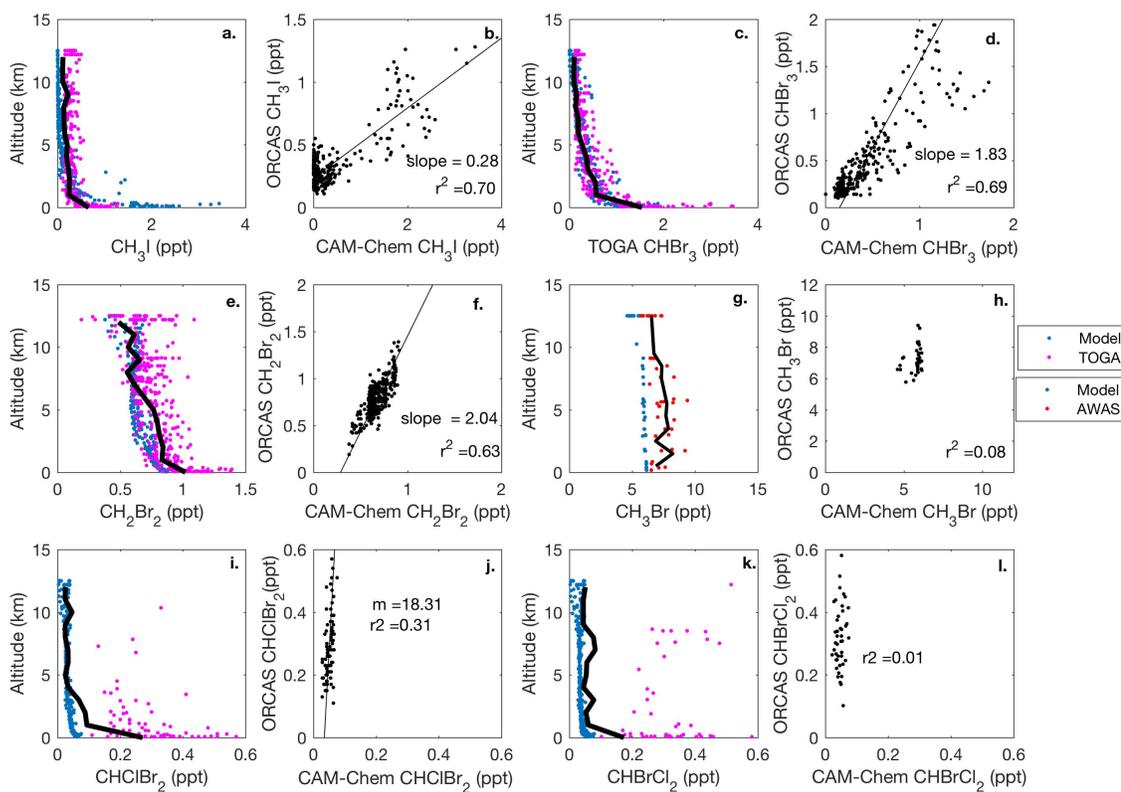
**Figure 6.** CAM-Chem 1.2 model-aircraft measurement (TOGA and AWAS) comparison during
ORCAS campaign between 1-12 km in Region 2, the Patagonian Shelf. All regressions are type
II major axis regression models bivariate least squares regressions (slopes are shown when the r^2
≥ 0.2). The bold, black line in each vertical profile represents the binned (mean) mixing ratio of
HVOC measurements at that altitude. Again, the binned mean includes measurements below the
detection limit (DL), which for this calculation are assigned a value equal to the DL multiplied
by the percentage of data below detection. Modeled values include locations where observations
were below the DL.

1058
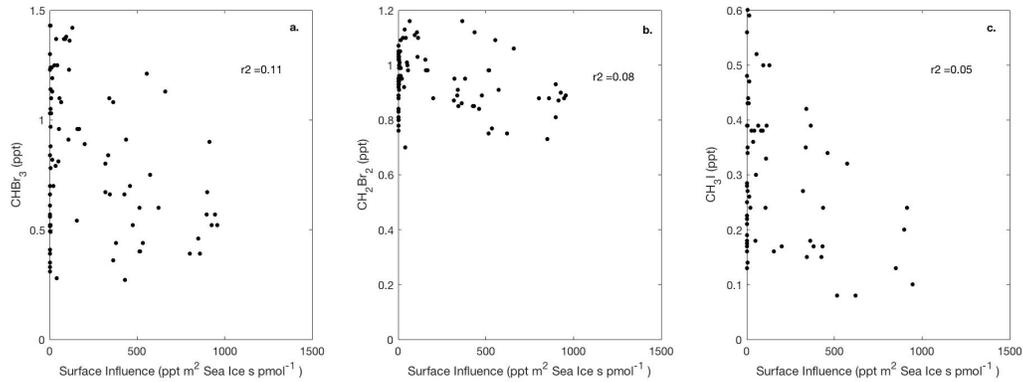
Figure 7. Linear type II regressions between influence functions convolved with sea ice distributions, which exclude land ice, and mixing ratios for $CHBr_3$, CH_2Br_2, and CH_3I in Region 1, poleward of 60° S. Surface influence (ppt m^2 s $pmol^{-1}$) in each grid cell was multiplied by fractional sea ice concentration surface field, which is unit-less, yielding sea ice surface influence function units of ppt m^2 s $pmol^{-1}$, as shown on the x-axis. Linear regression lines are not shown, as $p \geq 0.001$.
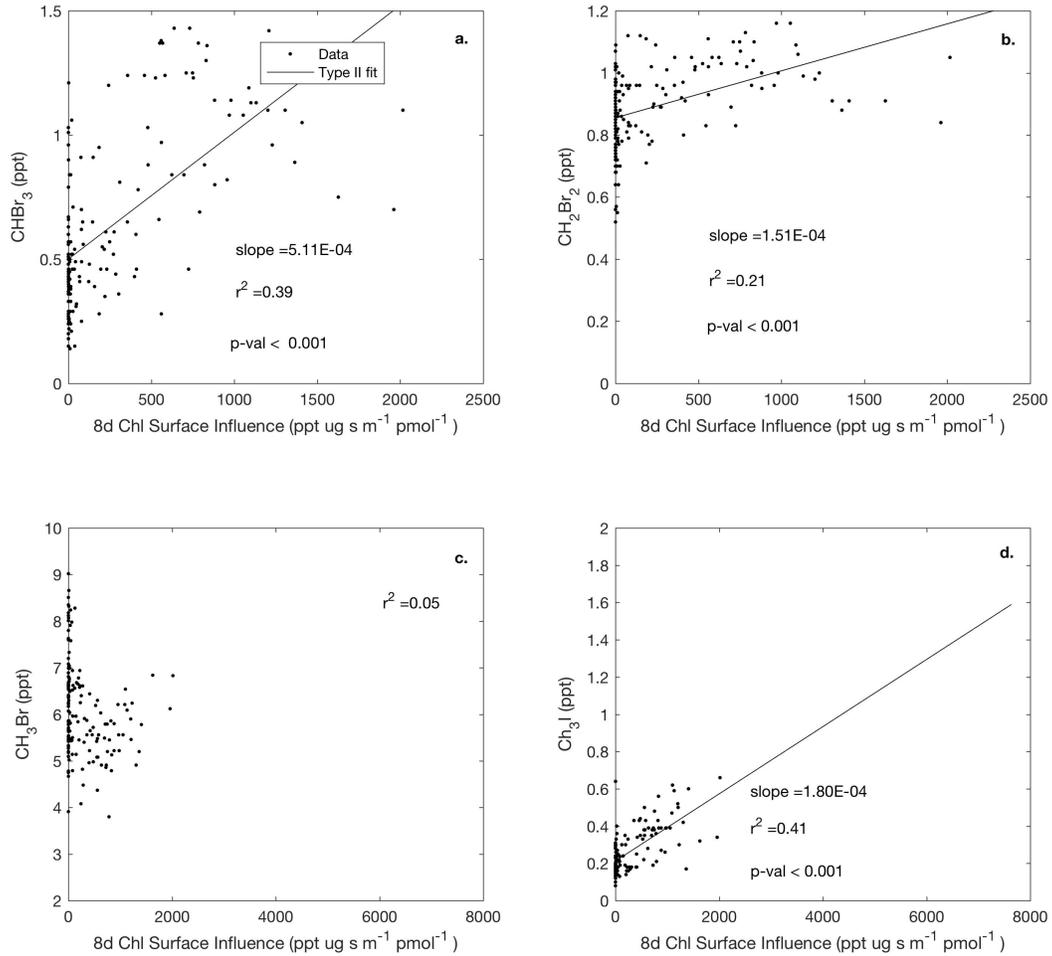
1066

1067

Figure 8. Linear type II regressions between influence functions of eight day composites of chl *a* and mixing ratios of HVOCs (a-d) poleward of 60° S (Region 1). Surface influence (ppt m^2 s pmol^{-1}) in each grid cell was multiplied by the chl *a* (µg m^{-3}) surface field, resulting in surface influence function units of µg ppt s pmol^{-1} m^{-1}, shown on the x-axis. Linear regression lines are shown where when p < 0.001.

1073

1074
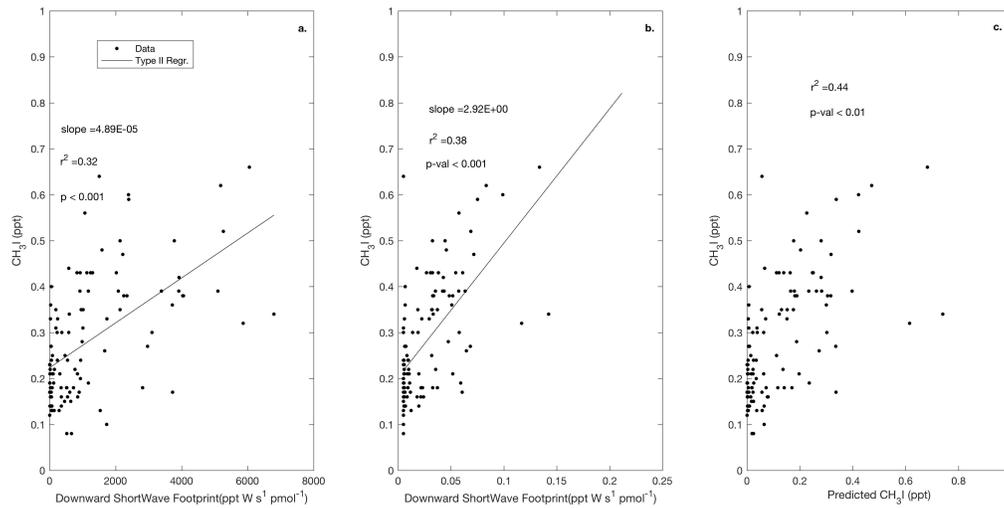
1075

Figure 9. Observed CH_3I plotted against the surface influence functions of downward shortwave radiation (a) and absorption due to detritus (b). Predicted mixing ratios of CH_3I based on a multiple linear regressions (MLR) using these two predictors in Region 1 are shown in Fig. 9c according to Equation 3. Surface influence (ppt m^2 s $pmol^{-1}$) in each grid cell was multiplied by the surface source field, such as shortwave radiation at the surface (W m^{-2}), yielding units of ppt W s $pmol^{-1}$, and the surface ocean's detrital absorption (m^{-1}), yielding units of ppt m s $pmol^{-1}$, shown on the x-axes.

1083
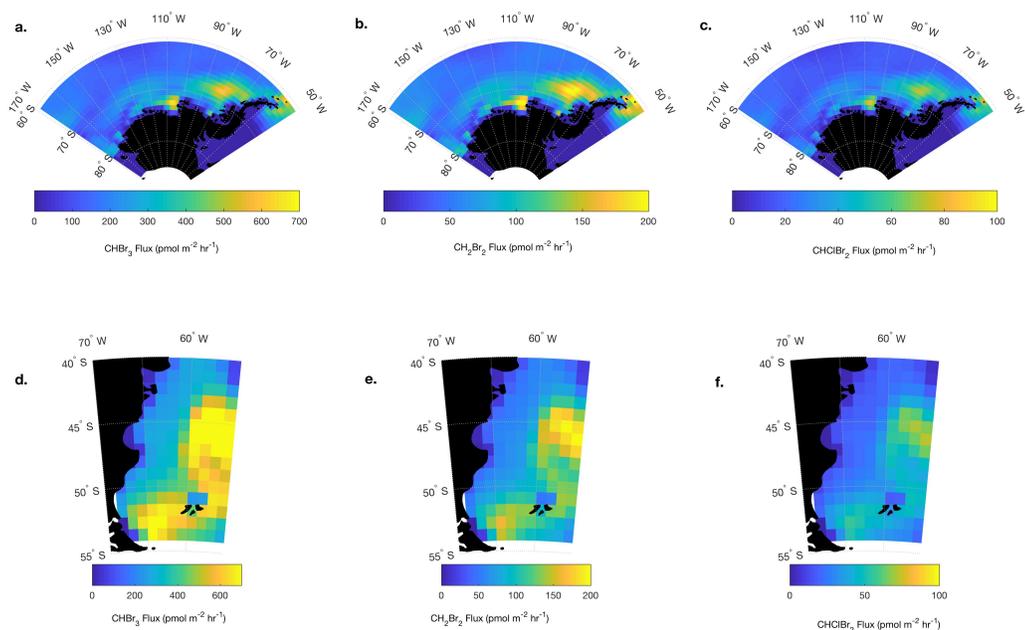
1084

Figure 10. Resulting mean Jan. – Feb. 2016 O_2-based (parameterized) $CHBr_3$ and CH_2Br_2 and $CHClBr_2$ fluxes (pmol m^{-2} s^{-1}) in Region 1 (a-c) poleward of 60° S and Region 2 (d-f) over the Patagonian Shelf. CESM modeled O_2 fluxes are scaled by the slope between the oceanic contribution to $\delta(O_2/N_2)$ and $CHBr_3$ and CH_2Br_2, and $CHClBr_2$ reported in Fig. 4. Note that these fluxes represent mean estimated biogenic fluxes in Jan. -Feb. 2016 (see Sect. 3.4.1 for details).

1090
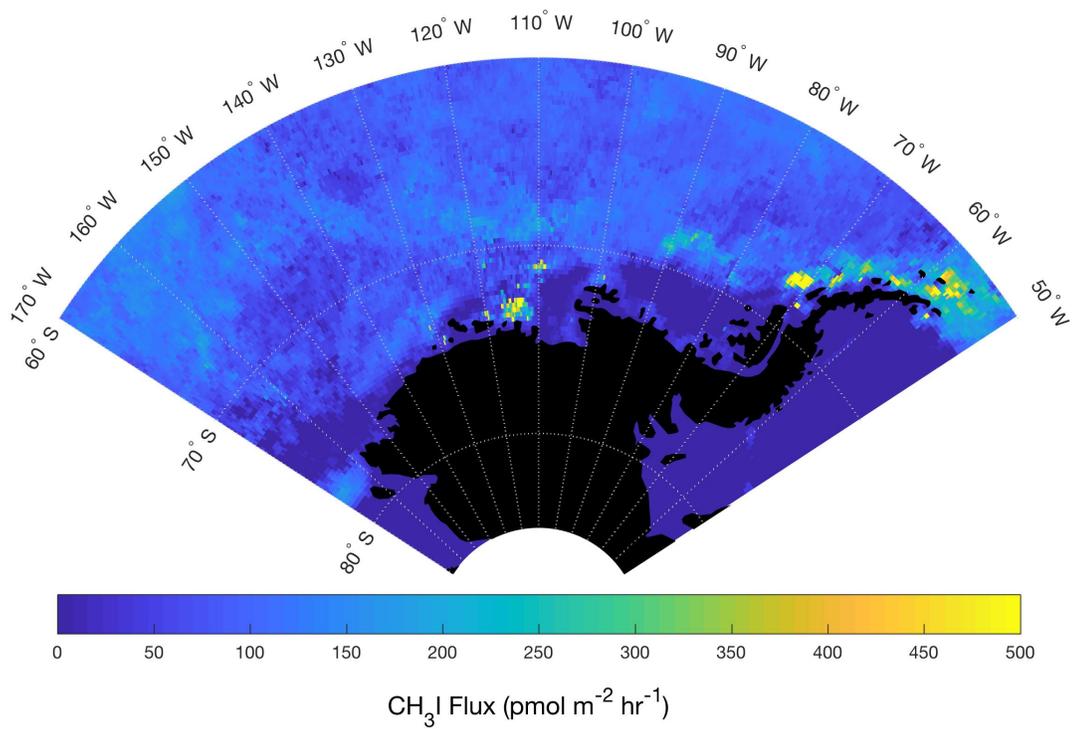
Figure 11. Mean estimated CH_3I fluxes for Jan. – Feb. The multilinear regression in Fig. 9 between CH_3I mixing ratios and geophysical influence functions related to shortwave radiation and detrital material at the sea surface was used to derive a mean flux field in Jan.-Feb., 2016 for Region 1.